

Abstract

Although carbonate reservoirs often have high total pore volumes, permeability often doesn't show a strong correlation to total porosity. Carbonate pore networks are also widely recognized as being highly heterogeneous, with marked variability in pore size (from sub-micron to millimetre scale and above) within an individual core plug. It is perhaps for this reason that there has been relatively little quantification of carbonate pore size and shape, despite significant advances in our ability to image naturally porous media using electron microscopy and advanced X-ray imaging.

This study focuses on four samples of limestone from the uppermost Shuaiba Formation in northern Oman. These samples were selected for X-ray CT and ESEM imaging and quantitative analysis following a detailed reservoir quality evaluation of the study interval across seven fields. This interval has been well-studied sedimentologically but the processes and timing of diagenetic modification, and the nature of the resultant pore network, are less well understood. The samples represent a range of lithofacies associations that occur immediately beneath the Shuaiba - Nahr Umr unconformity, within an interval that is recognized for possessing higher permeability than the underlying reservoir. The samples were imaged at multiple scales and their pore network analyzed.

Within the sample set, over 70% of the total pore volume is $< 1 \mu\text{m}$ diameter. The 3D equivalent pore radii within individual samples ranges from $< 0.1 \mu\text{m}$ to $> 100 \mu\text{m}$, the size of the X-ray imaged samples being limited to 1 mm^3 . The average aspect ratios of all pores was < 2 , and was highest in micropores ($< 1 \mu\text{m}$ pore radii). Mean co-ordination number was < 3 in all samples, and was highest within micropores. Since most pore throat radii are $< 1 \mu\text{m}$, this most likely reflects the higher resolution needed to image micropores. Multivariate analysis shows that permeability prediction is improved when pore topological parameters are known. The highest measured permeability within the dataset occurs in the sample with the highest volume of resolved porosity, highest aspect ratio and highest co-ordination number. However, average permeability overall is highest in those facies associations with abundant macropores, the representative elemental volume of which is greater than the sample size required for X-ray CT analysis and even routine core analysis. In these samples, high permeability is facilitated by a connectivity of a low volume of large ($>> 30 \mu\text{m}$) pores, embedded within a network of micropores. In these samples, sweep efficiency during hydrocarbon production is likely to be poor.

The results of this study provide one of the first detailed datasets of 3D pore shape and size within this volumetrically important reservoir and provides insight into pore connectivity within microporous reservoirs on the Arabian Plate. The results provide good evidence that the $>1\ \mu\text{m}$ fraction of these rocks contributes to single phase flow, but demonstrates the complexity of pore shape even at the micron-scale

Introduction

The Lower Cretaceous Shuaiba Formation is one of the most commercially important hydrocarbon reservoirs in the Middle East. Many studies have been conducted in order to understand and visualize the controls on its reservoir architecture, critical to the maintenance of oil production in Northern Oman. These studies have been driven by the need to understand the sedimentological complexity of the Shuaiba Formation, and the impact of this complexity on the storage and the flow of fluids. Significant heterogeneity derives from variations in depositional processes; therefore, several detailed outcrop studies (Masse et al., 1998; Immenhauser et al., 2001; Immenhauser & Scott, 2002; Immenhauser et al., 2004; Borgomano et al., 2002; Amthor et al., 2010; Buchem et al., 2010; Hillgärtner, 2010,) and subsurface studies (van Buchem et al., 2002; Droste, 2004; Droste, 2010; Warrlich et al., 2010) have been published. Nevertheless, diagenetic processes also control pore geometry and reservoir complexity in most carbonate reservoirs (Ahr, 2008; Hollis et al., 2010; Worden et al., 2018), and therefore underestimating the impact of diagenesis on petrophysical reservoir properties could considerably reduce confidence in the prediction of regional patterns of porosity distribution and fluid flow. Only a few studies have described the diagenesis of the Shuaiba Formation and how it modifies porosity (Al Sharhan, 1987; Moshier, 1989; Budd, 1989; Lambert et al, 2006; Al Furqani, 2008; Al Hajri, 2015).

The main objective of this study was to investigate the processes that were responsible for pore modification in the uppermost Shuaiba Formation, particularly below the contact with the overlying Nahr Umr Formation, in multiple fields in the northern part of Oman (Figure 1b; Al Hajri et al., 2015). The fields were chosen to represent a dip section from the platform top to the Bab Basin (i.e. proximal to distal part of the Shuaiba platform). The top 15 m of the Shuaiba Formation, beneath the Top Shuaiba Unconformity (TSU) has distinctly higher effective porosity and permeability compared to lower reservoir zones, making it important to reservoir management (eg. Warrlich et al., 2010). This paper focuses specifically on a quantitative characterization of the pore system within this top reservoir layer. It presents a detailed classification of pore types and then attempts to characterize their shape and size. This is one of the first studies to quantitatively describe pore geometry in 2D and 3D from multi-scale datasets within a single stratigraphic layer of carbonate reservoir, and to attempt to relate this geometry to geological processes.

GEOLOGICAL SETTING AND STUDY AREA

The Shuaiba Formation is Aptian in age (Masse et al., 1998; Schroeder et al., 2010) and conformably overlies the Barremian Kharab Formation (Figure 1a). Throughout the Lower Cretaceous, sedimentation on the southern Arabian Plate was strongly influenced by the development of the Bab Basin, an intrashelf basin that formed in the region of the present day UAE and north Oman (Droste, 2010; van Buchem et al., 2010; Figure 1b and 2a). The lower part of the Shuaiba Formation is dominated by Orbitolina packstone and wackestone. These are overlain by *Lithocodium/ Bacinella* facies which became dominant across the Arabian Platform in the Lower Aptian, most likely in response to changes in ocean chemistry associated with an Ocean Anoxic event (Rameil et al., 2012). Rudist-dominated communities became established on the top of *Lithocodium/Bacinella* build ups, resulting in depositional slopes of 0.5° to more than 30° (Droste, 2010a). Carbonate deposition was then terminated across most of the platform by a fall in relative sea level, and emergence for a period of more than 5 Ma, forming an erosional unconformity in the platform interior that becomes conformable toward the Bab Basin (van Buchem et al., 2010; Immenhauser and Rameil, 2011). The Shuaiba Formation is overlain by, and reservoirs sealed by, the Aptian Nahr Umr Formation, which forms the base of the overlying Wasia Group (Forbes et al., 2010) (Figure 1a).

DATABASE AND METHODS

This study is based upon subsurface dataset comprising about 244 m core and logs from 13 wells with conventional and special cores analysis (CCA and SCA). The cores capture the contact between the Shuaiba Formation and the overlying Nahr Umr Formation from seven fields in northern Oman labeled as A, B, G, H, L, M and R fields, (Figure 1b). The basal 1 - 4 m of the Nahr Umr Formation and the uppermost 10 to 15m of the Shuaiba Formation were described in detail (rock-texture, skeletal and non-skeletal allochems, pore types, and cementation, compaction and fracturing). Diagenetic features were described petrographically using transmitted light and cold cathodoluminescence microscopy. Modal analysis (point counting) was conducted using Petrog © software attached to a Nikon LU200 PCL microscope to quantify the macropore types, diagenetic and depositional components of 54 thin sections. 300 points were counted in each thin section at 4x magnification (Figure 2b). The core-based porosity measurement and the point-counted porosity were integrated and used to calculate the percentages of the matrix microporosity using the following simple equation:

Matrix microporosity= Core-based porosity – Total point counted porosity

Porosity was described using Choquette and Pray (1970). Different pore types (i.e. macro and micropores) were recognized and described in core and under the microscope using 214 thin sections.

Detailed characterization of micropores utilized scanning electron microscope (SEM), back-scattered electron microscopy (BSEM) and environmental scanning electron microscope (ESEM).

The shape and size of pores was extracted from binarized petrographical images generated by ESEM and BSEM using ImageJ ©. The complexity of the pore space in 2D was described by the value of perimeter over area (POA; see Anselmetti et al., 1998) and the pore equivalent radius (i.e. the radius of the best fitting circle within a pore space) according to:

$$\text{Perimeter over Area (POA)} = \frac{\text{Perimeter (P)}}{\text{Area (A)}}$$

$$\text{Pore Equivalent radius (EqRadius)} = \sqrt{\frac{A}{\pi}}$$

The pore diameter in 2D was calculated as the minimum distance between any two points within the pore space (i.e. Minimum Feret's diameter). Tortuosity (τ) was calculated as the ratio of the longest path of fluid flow (L_a) to the shortest distance between the two points which represent the entry and the exist points of the fluid (L).

X-ray CT analysis

Four samples were scanned using the Nikon Custom Bay scanner at University of Manchester, and scans of two of these samples were also taken at a higher resolution in the Micro- Xradia-XCT scanner at the Manchester X-ray Imaging Facility (Table 1). The samples were prepared as 1mm wide 'matchsticks' and bombarded by high energy X-rays. An offset correction was applied during sample calibration by taking an image of the detector with and without the sample. The transmission rate, which should be 20% - 25%, was calculated by dividing the image of the sample by the image of the detector. Further calibration included the source-detector offset adjustment. Filters were added during some scans to remove the low energy rays that may cause blurring of images. The exposure time and the energy level were adjusted to improve image quality. Generally, lower noise and greater edge detection can be obtained using higher energy and longer exposure times. The continuous images of each sample were converted to digital images using XMReconstructor © for the Micro- Xradia- XCT scanned samples and CT Pro © for the Nikon Custom Bay scanned samples. Image quality was improved during the reconstruction by reducing the impact of the bombarded X-ray beam on the induced variation in the intensity of the gray color from the surface, where high amount of x-ray energy is absorbed, to the center of the scanned sample, where the energy of the transmitted X-rays is comparatively low, are resulting in inconsistent variation in the intensity with darker areas at the surface and bright center.

To improve image quality, by reducing noise and sharpening the edges between pores and minerals, median and unsharp mask filters were applied using Avizo Fire © software (Figure 3). Application of the median filter reduced the noise by softening the edges of the objects while the unsharp mask filter sharpened the images without exaggerating the noise. Segmentation of pores from the solid minerals used the watershed technique in Avizo Fire enhanced the variation in intensity of grey level at the boundaries between phases and computation of morphological gradients (i.e. the edge detection) in 3D (Figure 3). The morphological gradients were then labeled and isolated from the remaining parts of the sample. This step was important as it allowed successive partitioning and quantitative thresholding of the other phases within the image without including the voxels of the transition area, creating an inverse image of the gradients. The values of grey level for the inverted image were then used as a mask during identification of the other phases which allowed more accurate segmentation. Finally, all the segmented phases and the transition zones were combined to construct the 3D model of the sample (Figure 3). The Sobel filter was used to define the boundaries between the phases instead of calculating the gradient in Avizo Fire because it gave a more accurate labeling for the boundaries. Manual segmentation was also applied where pores were complex. Each pore was labeled with a different color in order to perform statistical analysis and quantitative characterization of individual pores-

Following segmentation, Avizo Fire was used to calculate pore morphological parameters in 3D, including, bulk volume, pore volume, pore area, pore length and width, pore equivalent diameter (EqDiameter) (i.e. the diameter of the best sphere that can fit within the pore space which has the same volume) pore and pore throat radii. These parameters were used to calculate X-ray CT porosity (pore volume/bulk volume), dominant pore size, pore equivalent radius, and a number of pore shape descriptive parameters in 3D, including specific surface area (SSA) and aspect ratio. The terminology follows that of Weger et al (2009):

$$\text{Specific Surface (SSA)} = \frac{\text{Area in 3D (A)}}{\text{Pore Volume in 3D (V)}}$$

$$\text{Aspect Ratio (AR)} = \frac{\text{Pore length (L)}}{\text{Pore width (W)}}$$

The dominant pore size for each sample was calculated as the pore size below which 50 % of the porosity calculated from the images is composed (Weger et.al, 2009).

The pore shape, size and orientation were visualized and the pore network reconstructed using the centerline tree module in Avizo Fire. This module generates lines at the centre of the segmented

pores, which are visualized as tubes with variable thicknesses depending on the mean distance between the centre lines and the walls of the surrounding pore. The coordination number of each pore was calculated using Matlab code. All pores with equivalent radius less than or equal to 1 μ m were considered as micropores. Pores with equivalent radius between 1 μ m and 30 μ m are referred to as mesopores whilst macropores are >30 μ m. Tortuosity (τ) was estimated for all samples with 3D X-ray CT data by calculating the length of the path that connects the points which represents the average position of all pores in each image in the z-axis and dividing this length by the total number of images along the z-axis.

RESULTS

Lithofacies

Five lithofacies associations (LA) were defined from the database, consistent with previous work (Warrlich et al., 2010). Each LA comprises lithofacies that were defined based on texture, grains size, skeletal components, sedimentary structures and diagenetic features. The abundance of skeletal and non-skeletal allochems was estimated in thin sections using Bacelle and Bosellini (1965) charts referred to as trace (<1%), minor (1-5%), common (5-15%) and dominant (> 15 %) or by modal analysis (Figure 2).

Mudrock Lithofacies Association (MLA):

The MLA is found only in the Nahr Umr Formation, in Fields B, G, H, M and R and is made of dark green-grey, thinly laminated, fissile clastic mudrocks with trace, reworked, thin-shelled skeletal components, mostly molluscs (Figure 4a). Beds are a few centimeters thick. Pyrite is common and occurs as mm-cm sized nodules or irregular aggregates of euhedral and framboidal pyrite. It is found within the matrix and replacing thin shelled bivalves. The fine-grain size, abundance of clastic material and presence of bivalves suggest deposition in a low energy marine setting. The presence of pyrite in the mudrocks indicates oxygen reduced conditions either within the water column or immediately below the sediment water interface.

Rudist Lithofacies association (RLA)

The RLA comprises rudist rudstone, rudist floatstone, rudist-rich skeletal floatstone and skeletal packstone to grainstone, (Figure 2 and 4c-d). The RLA typically occurs at the top of the Shuaiba Formation, beneath the unconformity with the Nahr Umr Formation. Often, biomoulds formed by rudist dissolution are partially filled by mudrock of the overlying Nahr Umr Formation (Fields A, G, H, B and M). It occurs stratigraphically above the *Bacinella*-dominated lithofacies and ranges from 10s of centimeters to 12m thick, in Field H. The RLA is dominated by rudist bivalves and trace to common

benthic foraminifera, particularly *Orbitolina*, and common peloids. Sorting is very poor and the matrix has an inhomogeneous fabric with patchy distribution of micrite. Boring and fragmentation of rudists are common, especially in grainstone to packstone lithofacies.

The presence of large rudist bivalves suggests deposition in shallow warm waters with high levels of light penetration, (Masse et al., 1998; Malchus et al, 1995; Flugel, 2004). The association with benthic foraminifera and *Lithocodium/Bacinella* indicates deposition within a shallow, gently agitated lagoonal environment with periodic fragmentation by wave and storm activity (Figure 4d). Correspondingly, this lithofacies association is thickest and most abundant in the most proximal fields (A and G), although it also dominates within Field H.

Bacinella Lithofacies Association (BLA):

This lithofacies association comprises *Lithocodium/Bacinella* boundstone and floatstone, *Lithocodium/Bacinella* -rich skeletal floatstone, skeletal packstone and wackestone, (Figure 2 and 4e-f). It is common in Fields A, G, B, M and R and varies from 10s of centimeters up to 10 m thick. The BLA is dominated by *Lithocodium/Bacinella* algae and trace to minor *Orbitolina*, skeletal debris, echinoderm, miliolid, biserial textularide and bivalves with minor or trace peloids. Facies are very poorly to poorly-sorted and the matrix has an inhomogeneous fabric with a patchy distribution of micrite. The boundstone lithofacies, which are composed of laminar *Lithocodium/Bacinella*, occur in Field A, which has the thickest *Lithocodium/Bacinella* units (up to 10 m). Further north, thinner, patchy and clotted *Lithocodium/Bacinella* morphologies are dominant (Fields G, M and R), with only a few patches of *Bacinella* in Field B, within the *Orbitolina* lithofacies. The BLA is not found in Fields H and L. Massive to laminar *Lithocodium/Bacinella* were probably deposited in a low energy shallow marine setting where sedimentation rate was low, whilst patchy and cloudy *Lithocodium/Bacinella* more commonly formed where the rate of sedimentation and oxygenation was higher (Rameil et al, 2010). Correspondingly, the dominance of laminar *Lithocodium/Bacinella* boundstone in Field A is consistent with its more proximal position on the platform, with a transition to patchier forms basinward (Fields G, M and R). This LA is not found within the Bab Basin, as water depths were too high.

Orbitolina Lithofacies Association (OLA)

The OLA comprises *Orbitolina*-dominated lithofacies with packstone, wackestone and mudstone textures (Figure 2 and 4g-h). It occurs below, or intercalates with, the BLA in Fields A, M and R, but it is thickest where BLA is rare or absent. Overall, the OLA-dominated units range from 10s of centimeters up to 10m thick. They contain dominant to common conical and discoidal *Orbitolina* foraminifera, with a change in the morphology of the *Orbitolina* from discoidal to conical forms up-section, toward the *Lithocodium/Bacinella* and Rudist-dominated units. Other grains include trace to

minor miliolids, uniserial and biserial textularide foraminifera, minor to common thin-shelled molluscs, skeletal debris, and trace to common echinoderm debris. Peloids have a trace to minor abundance. The OLA has a moderately to poorly-sorted texture and the matrix has an inhomogeneous to clotted fabric with patchy distribution of micrite.

Orbitolina are large benthic foraminifera that were common in inner and outer platform settings throughout the Aptian, and which were typically deposited in a shallow water, lagoonal setting (Flügel, 2004; Pittet et al, 2002; Vilas et al 1995; Raspini, 1998). The change in morphology of the *Orbitolina* from discoidal to conical forms probably reflects an increase of water energy and increased light penetration. Fragmented skeletal debris indicates periodic high energy conditions, perhaps during storms, but overall depositional energy was low. It is most abundant in Fields B and R, which occur in a mid-platform position.

Benthic Foraminifera Lithofacies Association (BFLA)

The BFLA only occurs in the top 12 m of Field L, on the margin of the Bab Basin. It comprises an upward-cleaning and coarsening succession of foraminiferal wackestone to packstone, (Figure 2 and 4b) with common miliolid, biserial textularide and uniserial foraminifera and trace to minor bivalves, fragmented *Dasycladaceae* algae, skeletal debris and echinoderm fragments. Peloids are common, and there are traces of minor oncoids and reworked aggregate grains of foraminifera, especially within the wackestones to packstones. The matrix has an inhomogeneous and bioturbated fabric with common *Thalassinoides* burrows.

The dominant mudstone to wackestone texture with frequent burrows indicates deposition under low energy but well-oxygenated conditions. The diverse foraminiferal assemblage, including reworked aggregate grains, suggest deposition in an open marine environment, with the upward-cleaning and better sorted texture indicative of deposition under higher energy, shallower water conditions up-section.

Pore destructive diagenesis

The principal processes governing pore destruction within the Shuaiba Formation in the study area are calcite cementation (Fig. 5a – c) and chemical compaction, in the form of clay seams and stylolites. The most common calcite cements are blocky to drusy non-ferroan calcite that fill intraparticle pores in *Lithocodium/Bacinella* (Figure 5b) and partially fill moulds and vugs within the rudist dominated lithofacies (Figure 5a and c). Equant, very fine to finely crystalline, non-ferroan calcite also occurs within interparticle pores in the RLA, OLA and BLA. Rare syntaxial overgrowths of non-ferroan calcite are nucleated on echinoid fragments and rare fibrous to bladed, non-ferroan calcite lining the *Lithocodium/Bacinella* chambers and interparticle pores.

For ~8 m beneath the Aptian-Albian unconformity, the volume of cements is <10% before increasing to ~20% (Figure 6a; Table 2). The highest volume of cement occurs within the BLA with floatstone and boundstone textures (12.0%; 1.3 - 28.0 %). The RLA contains an average 9.0% cement (0.7 - 22 %) while the OLA comprises 6.1% (0.3 – 14.7 %). Porosity degradation also occurs by neomorphism of the micritic matrix and some allochems. In stained thin sections, the neomorphosed matrix has a pink stain indicative of non ferroan calcite (Figure 5B). It is most pervasive in the RLA (17.8 %; 0.0 – 43.3%) with lower volumes in the OLA (8.9 – 22.3%) and BLA (9.9%, 0.0 – 19.0%). Neomorphism is most pervasive in the uppermost 5 m of the Shuaiba Formation (>>20%), decreasing to <15% at ~10%, before increasing to ~20% (Figure 6b).

Macroporosity (>30 µm)

Primary interparticle pores occurs between grains but it is rare that it is observed without further modification (< 3.0 %; Figure 6c and 7a, Table 2). Petrographic observations suggest solution enlargement of these interparticle pores adjacent to core- and microscopic-scale fractures (Figure 7a). Intraparticle pores occurs within grains and can be either primary or secondary. This type of porosity displays a patchy distribution and occurs principally within benthic foraminifera and *Lithocodium/Bacinella* (Figure 7b, Table 2). Moldic pores occur primarily in the upper 4 - 6 m of the Shuaiba Formation, principally in the RLA (Figure 6d, Table 2) with its highest occurrence in Fields A (9.7%, 2.3 – 16.0 %), B (9.9 %, 3.3 – 26.7 %) and G (11.0 %, 1.7 – 21.0%; Table 2). Moulds are formed by rudist dissolution (Figure 7c), are up to 4cm in size and can also form by partial to complete dissolution of micritised skeletal allochems and peloids (Figure 7d). Volumes of vuggy (i.e. non-fabric selective) porosity are low overall (< 5% average) but are > 5% in the RLA for up to ~5 m beneath the Shuaiba – Nahr Umr unconformity (Figure 6e, Table 2).

Fracture porosity occurs in partially calcite-cemented or open fractures, some of which have irregular margins. Fractures range from 10µm to ~ 1 cm wide and a few cm to 1.5 m long, tending to be longer and wider in grain-dominated, moderately to highly cemented lithofacies such as the RLA and BLA. In comparison, the mud-dominated, poorly cemented lithologies (OLA and BFLA) are characterised by short and narrow fractures. Solution-enlarged stylolites occur where dissolution has taken place along stylolites and compaction seams, creating enlarged seams that are a few 10s of µm to 100s µm wide (Figure 7c). Combining fracture volumes with mouldic and vuggy pores shows a high volume of secondary macropores (>20%) in the RLA and OLA for up to ~10 m beneath the top Shuaiba unconformity (Figure 6f).

Mesoporosity (1-30 microns) and microporosity (<1 µm)

Meso- and microporosity takes several forms. Primary matrix meso- and microporosity is pore space between euhedral to subhedral micrite crystals (Figure 8a). Secondary matrix meso- and micropores occur where primary meso- and micropores have been enlarged, often adjacent to solution enlarged fractures and stylolites (Figure 8b). One of the most visible pore types is micro-peloidal moldic pores, where individual pores are less than or equal to 10µm in diameter (Figure 8b) and are particularly prominent in Fields A, G, B and L. Secondary intraparticle meso- and micropores, formed by the dissolution of the micritic part of skeletal allochems (particularly *Orbitolina*, small benthic foraminifera and *Lithocodium/Bacinella*) is most common within the BLA and OLA, especially in Fields B and M as well as within RLA where it is inter-bedded with OLA in Fields H and G.

Reservoir quality

The relationship between porosity, permeability, well location, lithofacies and depth is shown in Figure 9. Overall, porosity ranges from 20 – 40%, and permeability from 1 - < 50 mD (Figure 9a), but porosity and permeability are notably higher in Fields G and A (>35 % and > 50mD), and lower in well H2 (< 20% and < 1mD; Figure 9b). Overall, porosity and permeability are highest in the RLA, with porosity also being more effective in this facies association (i.e. permeability is higher for a given porosity compared to other lithofacies associations; Figure 9a). Nevertheless, this facies association also has the lowest porosity and permeability in well H2 (Figure 9a-b). In general, permeability is higher for a given porosity in the BLA compared to the OLA (Figure 9b). In Fields A, L, R, H and M, there is no clear trend in total porosity beneath the Shuaiba - Nahr Umr unconformity, but permeability decreases gradually downwards (Figure 10). In Fields B and G, porosity and permeability generally decrease with depth, but there is some variability between facies. Typically, porosity is lower and permeability higher within the RLA in these fields compared to the OLA and BLA, although in well G2 porosity and permeability are much lower in the RLA than the BLA (Figure 10). In Field R, both porosity and permeability are relatively trendless (Figure 10). In summary, porosity is fairly trendless, but permeability typically decreases downwards beneath the top Shuaiba unconformity, regardless of facies and absolute permeability, but this trend is usually strongest where the RLA occurs beneath the unconformity.

Pore geometrical data

The samples imaged by X-ray CT and ESEM have total porosities ranging from 23% (L1) to 35.6% (M1; Figure 11, Table 3). Permeability is highest in sample L1 (34.5mD) and lowest in sample M1 (5.2mD; Table 3). The volumes of porosity captured during X-ray CT analysis are summarised in Table 3, and presented as unresolved porosity (i.e. (Helium porosity – measured pore volume)/Helium porosity)*100). There is an increase in the volume of total porosity imaged with an increase in the

resolution of the image; the unresolved porosity using the Custom Bay ranges from 69.9% to 99.8 % of the total core porosity, decreasing to 74.5-92.6% on the Micro-XCT (Table 3). Within the ESEM dataset, < 40% pore volume is unresolved, and in two samples there is more porosity resolved than was measured by routine core analysis (Table 4). Equivalent pore radius decreases from Custom Bay to Micro-XCT to ESEM (Figure 12) and correspondingly, the dominant pore size decreases between images from the Custom Bay (> 10 μm), Micro-XCT (> 1 μm and < 10 μm) and ESEM (<< 1 μm ; Table 3-4, Figure 13a-b). Aspect ratio in all samples is < 10, and in all case averages < 2 (1.6-1.9), increasing slightly as sample resolution is increased and dominant pore size decreases (Figure 13c-e). Specific surface area varies from 0.140 to 0.431 μm^{-1} , being highest in sample G1 and lowest in sample L1 (Figure 13f, Table 3). Co-ordination number was determined on the 3D datasets and mean values range from 1.08-2.41 in Custom Bay data, increasing to 2.14-2.49 on the two samples imaged using the Micro-XCT (Table 3, Figure 13g). Mean tortuosity decreases from the highest values in samples analysed on the Custom Bay to lower values in samples imaged on the Micro-XCT and by ESEM, except in sample L1 (Figure 13h).

Mean specific surface area (SSA) is inversely related to mean equivalent pore radius ($R^2= 0.91$, $R_{\text{adj}} = 0.73$ for the Custom Bay images; Figure 14a). The mean calculated tortuosity (τ) from X-ray CT images increases as mean specific surface area increases and decreases with increasing aspect ratio, with a stronger coefficient of determination for the 3D compared to the 2D ESEM images (e.g. R^2 for tortuosity versus aspect ratio is 0.60, with R_{adj} showing no correlation for the 2D images and $R^2= 0.93$, $R_{\text{adj}} = 0.70$ for the for the 3D images; Figure 14b-c). Tortuosity also decreases with increasing aspect ratio ($R^2= 0.91$, $R_{\text{adj}} = 0.75$; Figure 14c) and, to a lesser extent, co-ordination number ($R^2= 0.73$, $R_{\text{adj}} = 0.21$; Figure 14d).

Comparing data collected on the Custom Bay, the highest volume of porosity was resolved in sample L1 (BFLA, 69.9% unresolved porosity) and the least in sample G1 (RLA, 99.8% unresolved porosity; Figure 13a; Table 3). Sample M2 (BLA) has the largest dominant pore size (49.6 μm) and L1 the smallest (29.5 μm ; Figure 13b). The highest average SSA (0.431 μm^{-1}), near-lowest average pore equivalent diameter (15.7 μm , almost equal to M2 = 15.2 μm) and lowest average aspect ratio (1.67) are within G1, whilst M2 (BLA) has the lowest average SSA (0.140 μm^{-1}) and highest average pore equivalent radius (28.6 μm ; Figure 13). Average aspect ratio is >1.8 in all samples except G1. Average co-ordination number is highest (2.41) and tortuosity lowest (3.22) in sample L1, whilst average co-ordination number is lowest in sample G1 (1.08), which also has the highest tortuosity (34.6) (Figure 13).

The two most microporous samples, G1 and M1, were imaged using the Micro-XCT. This increased the volume of resolved porosity to 9% of the rock volume (from 0.1%) in sample G1 and to 2.7% (from 0.9%) in M1. Mean dominant pore size was slightly larger in G1 than M1 (5.32, cf 4.37 μm), with 3D equivalent pore radius also slightly larger in G1 (7.1 μm) compared to M1 (5.3 μm) (Figure 12 and 13a-b). Correspondingly, G1 has a lower mean SSA (0.983 μm^{-1} cf 1.12 μm^{-1}) and lower mean tortuosity (3.53 cf 2.65) than M1 (Table 3). There is little difference between the mean aspect ratio (1.73) and mean co-ordination number (2.49) in G1 compared to sample M1 (1.68 and 2.14, respectively) (Figure 13c-e and g)

From the ESEM database, 3D equivalent pore radius (Figure 12), mean dominant pore size (0.267 – 0.357), mean perimeter over area (16.9-29.1) and mean aspect ratio (1.87-1.91) vary little between samples (Figure 13, Table 4). Mean tortuosity is lowest in sample G1 (1.22) and highest in L1 (5.74) (Figure 13h).

INTERPRETATION

Controls on reservoir quality

Cross-plotting porosity and permeability for the entire dataset shows that permeability is highest in the RLA, although total porosity is similar to the BLA and OLA (Figure 9a). This indicates that porosity within the RLA is usually more effective, consistent with a high abundance of large, solution-enhanced biomoulds. These biomoulds were formed primarily by dissolution of coarse grained aragonitic rudist debris, with further solution-enhancement next to fractures. The biomoulds and vugs are particularly abundant within the uppermost 8 m of the Shuaiba Formation (Figure 6d-f), where total secondary macropores can exceed 20% of the rock volume (Figure 6f) and permeability can be up to an order of magnitude higher than in underlying beds. The RLA was deposited in clear, shallow water, often atop laminar *Lithocodium-Bacinella* boundstone, and it therefore it dominates in the southern, more proximal part of the study area. Nevertheless, cementation can degrade reservoir properties, and the lowest porosity and permeability for the entire dataset is within the RLA in well H2 (Figure 9a and 10), where pore filling calcite cements are abundant.

The BLA has undergone significant solution enhancement of intraparticle macropores to form vugs that can connect to give permeabilities of >10mD (Figure 9a). Although average total secondary macroporosity in this lithofacies association is only slightly lower than for the RLA (11.2%, cf 12.8%; Table 2), pore sizes are smaller and less well connected. There is also no demonstrable relationship between total pore volume and depth beneath the top Shuaiba unconformity for either this facies association or the OLA, although a slight increase in permeability can occur (Figure 10). Permeability in the OLA is lower than the BLA since macropores are dominated by small, poorly connected

intraparticle macropores and average total secondary macropore volumes are lower (7.9%; Table 2). There is no clear spatial variability in reservoir properties within these lithofacies associations, although total porosity and permeability is higher in Field M compared to Fields B and R (Figure 9b) due to a lower volume of pore filling cements (average 1.9%; Table 2).

There is no clear relationship between lithofacies association and the volume of pore filling cement (Table 2), but the volume of replacive spar is notably higher in the RLA compared to other facies associations. Total volumes of cement and replacive spar are highest in Field G (12.6 and 15.5% respectively), reflecting the dominance of the RLA in this sample set. Overall, however, the strongest control on the spatial variability of cements is depth beneath the top Shuaiba unconformity. In general, cement volumes are lowest (mostly <10%), in the uppermost 8 m of the Shuaiba Formation, (Figure 6a) whilst the volume of replacive spar is greatest (>10%) in this same interval, particularly within the RLA (Figure 6b). It is beyond the scope of this paper to evaluate the reasons for this, but it is possible that there is a genetic link between secondary pore generation and matrix neomorphism.

Overall, although depositional facies influence reservoir properties, only small volumes of primary macropores are preserved, and therefore the controls on reservoir quality are entirely diagenetic. The best reservoir quality occurs within the uppermost 8 m of the Shuaiba Formation, particularly in the RLA, in the southern, most proximal part of the study area, through solution-enhancement of the macropore network. This has formed large, well connected vugs and biomoulds and created an effective macropore network, albeit set within a neomorphosed matrix. In the BLA and OLA, primary macropores are dominantly intraparticle. The size of these pores has been enhanced by solution enlargement, but pores are smaller and less effective than for the RLA. Although there is no obvious increase in the volume of secondary macropores beneath the TSU for the BLA or OLA, cement volumes are much lower in this interval. Consequently, permeability is usually higher within the upper 8 – 10 m of the Shuaiba Formation than in underlying beds of the same facies.

Pore size

There are a wide range of definitions of pore size, but for the purposes of this study, macropores are considered to be all pores >30 μm (ie. can be resolved in thin section and X-ray CT scans), mesopores are >1 μm and <30 μm (ie. can be resolved by X-ray CT scans) and micropores are < 1 μm and can only be resolved using ESEM. Analytical limitations mean that to ensure a resolution of a few μm diameter by X-ray CT analysis, sample size must be ≤ 1 mm.

The quantitative analysis of X-ray CT data and image analysis of ESEM images reveals a wide range of pore sizes, although >70% of pores in all samples are < 1 μm diameter. This emphasises the importance of micropores to the pore network within the entire dataset, even within the highest

permeability facies. ESEM observations show that these micropores are intercrystalline, between micrite particles, and often appear to be solution enhanced (Figure 8). Strikingly, there is significantly less variation between samples in the size of micropores than in meso- and macropore size (Figure 12).

Although the RLA has the largest, best connected macropore network, based on core and thin section observations, it has the highest volume of unresolved porosity under X-ray CT analysis within this sample set (Sample G1, 99.8% microporosity). Macropores within this lithofacies association are typically cm-scale, visible in core with the naked eye, and therefore they could not be captured in the imaged sample, which was $< 1\text{mm}^3$. The Custom Bay data shows that sample G1 has very low volumes of mesopores, a high average SSA ($0.431\mu\text{m}^{-1}$), small pore equivalent radius (Figure 12), low mean coordination number (1.08) and high mean tortuosity (34.6) (Figure 13). Imaging the pore network at a higher resolution, using the Micro-XCT, resolves more mesopores (74.5% unresolved porosity; Table 1, Figure 12), with a mean dominant pore size of $5.32\mu\text{m}$, a higher mean co-ordination number (2.49) and lower mean tortuosity (3.46) than the lower resolution scan (Figure 13). Under ESEM, all pores are resolved, with a mean dominant pore size of $0.329\mu\text{m}$ (Figure 13) and a multimodal equivalent 3D pore radius distribution within micropores (Figure 12). In summary, this sample has a complex network of large (mm-scale) macropores embedded within a microporous network, with less abundant mesopores than samples from other lithofacies associations. Consequently, although the macropores are well connected, the small average size of the supporting matrix meso- and micropore network means fluid flow through the rest of the sample is tortuous.

Sample M2 has the largest mean dominant pore size ($49.6\mu\text{m}$) and 3D equivalent pore radii are mostly $>10\mu\text{m}$ (Figure 12) based on Custom Bay data, although 91.5% porosity was unresolved. Using ESEM, 38.9% porosity was unresolved, with the smallest mean dominant micropore size ($0.267\mu\text{m}$) of all the samples. The Custom Bay X-ray CT scanner imaged most pores in sample L1 (unresolved porosity, 69.9%), which has the smallest mean dominant pore size ($29.5\mu\text{m}$) and a relatively narrow range of 3D equivalent radius (almost entirely $>10\mu\text{m}$; Figure 12); i.e. the resolution of this scanner was optimal for the pore size range of the sample. A high volume of microporosity was imaged by ESEM (39.6%), with a mean dominant pore size of $0.35\mu\text{m}$, and all imaged pores are $> 0.01\mu\text{m}$ (cf other samples in Figure 12). This suggests that sample L1 has a narrower range of pore sizes, and therefore less heterogeneity, than other samples.

In sample M1, 97.4% of porosity was unresolved by the Custom Bay scanner and 92.6% was unresolved by the Micro-XCT. It has a small mean dominant mesopore size ($4.37\mu\text{m}$), the lowest 3D equivalent pore radius (Figure 12) of all samples and a high specific surface area (average $1.120\mu\text{m}^{-1}$). Under

ESEM, ~5% porosity is unresolved, and dominant pore size is similar to samples G1 and L1 (0.339 μm), implying a more microporous pore network than other samples.

Pore shape

In order to compare pore shape between the 3D and 2D datasets, aspect ratio is used to describe pore morphology. ESEM data reveals that micropores have higher aspect ratios than meso- and macropores, with a relatively consistent range (1.87 – 1.93; Table 2, Figure 13e). Samples L1, M1 and M2 comprise intraparticle meso- and macropores and biomoulds, some of which have been solution-enhanced, and have an average aspect ratio of 1.81-1.88. The lowest average aspect ratio (1.67) is in sample G1, in which the imaged meso- and micropores are dominated by biomoulds after foraminifera. This would suggest that biomoulds and intraparticle macropores are the most spherical pores, whilst solution enhancement of primary and secondary macropores, including fractures, creates flatter pore shapes. Although the largest solution-enhanced macropores could not be captured by X-ray CT analysis, in sample G1, visual inspection of thin sections would support this conclusion. For example, in Figure 7, the largest pores have a high length-width ratio.

Pore connectivity

Pore throat radius was determined from MICP analysis (Figure 12). All samples show a consistent pore throat diameter of ~ 0.1 to ~ 10 μm . The widest pore throats occur in sample G1, with the narrowest pore throats in sample M1 (<1 μm), the most microporous sample. Importantly, MICP data does not appear to capture the smallest pore throats, since micropores imaged by ESEM are smaller than most pore throat radii measured from MICP data.

Sample L1 has the highest permeability (34.5mD), the highest co-ordination number (2.41), the lowest tortuosity (3.22) and the narrowest range of pore sizes. Mean co-ordination number is lower and tortuosity higher in samples M2, M1 and G1. Permeability is higher in M2 than G1, as would be expected by these parameters. M2 also has a higher range of pore throat diameters (up to nearly 10 μm), compared to samples G1 and M1. Permeability in G1 is higher (13.9mD) than sample M1 (5.2mD), consistent with its larger mean dominant pore size, slightly wider pore throats (all pore throats > 1 μm diameter in G1 compared to ~ 90% in M1) higher co-ordination number, lower specific surface area and lower tortuosity based on the X-Radia XCT data (Figure 13, Table 3).

The positive correlation between tortuosity and SSA (Figure 14) indicates that as pore-size complexity and surface area increases, flow paths become more tortuous. Conversely, an increase in co-ordination number will facilitate a more direct fluid pathway, and therefore tortuosity decreases as pore connectivity improves. As more pores are resolved, at higher image resolution, co-ordination number increases and tortuosity decreases (Figure 12) indicating that meso- and micropores are well

connected. Pore shape is also important, with flatter pores (higher aspect ratio) facilitating more connectivity between pores, reducing tortuosity.

Calculation of permeability

Total core porosity correlates with permeability ($R^2=0.839$), but otherwise no single parameter correlates with permeability. Nevertheless, knowledge of pore shape and size can improve permeability prediction significantly (Archilha et al., 2016) and so a multilinear regression was constructed to assess the influence of different pore morphological parameters on permeability (Table 5). Using the 3D Custom Bay dataset, individually including tortuosity and specific surface area marginally improved R^2 (0.88 and 0.86 respectively), whilst the addition of dominant pore size improved R^2 to 0.90. The best correlation was achieved through the combination of total porosity and tortuosity ($R^2=0.99$). Consequently, predicted permeability shows the best match to actual permeability when dominant pore size, tortuosity and specific surface area are considered.

DISCUSSION

Spatial distribution of porosity

Many carbonate rocks do not show a strong relationship between porosity and permeability, principally as a result of diagenesis. This has resulted in a number of workflows by which rock types with specific petrophysical rock types can be defined, including methods focused on grain size and pore type (Lonoy, 2006, Lucia, 2007), geological flow units (Gunter et al., 1997; Ahr, 2008) and integrated geological and petrophysical characterisation (Hollis et al., 2010; Skalinski and Kenter, 2015). There are advantages and disadvantages to each of these approaches (see summary in Skalinski and Kenter, 2015), but the method preferred here is to consider the actual pore network of the rock to be the result of a sequence of specific diagenetic events operating on individual facies (Hollis et al., 2010). In this way, the depositional template, which governs diagenesis at or immediately following deposition, is preserved, but each pore network is then determined to be the product of a particular pore evolutionary pathway. From here it should be possible to understand and predict the spatial distribution of pore networks, as a function of their respective diagenetic evolution.

Broadly, reservoir properties vary across the study area as a result of environmental controls on facies distribution. The RLA preferentially developed at the top of upward-shallowing sequences, overlying *Lithocodium-Bacinella* build-ups, primarily in the southern, most proximal part of the study area. *Lithocodium-Bacinella* thrived during deposition of the Shuaiba Formation during the Aptian, with the thickest deposits in the shallowest water areas, and so the BLA is most abundant towards the south to central parts of the study area. Since *Orbitolina* foraminifera can adjust their morphology to survive

under lower light conditions more effectively than other photosynthetic organisms, the OLA was deposited in slightly deeper water and more distal settings towards the Bab Basin.

It is beyond the scope of this paper to fully describe the diagenetic evolution of each facies within this study; this is discussed in Al Hajri (2015). The dataset shows, however, that although there is an overall variability in rock properties between lithofacies associations, the controls on porosity, pore topology and permeability are almost entirely diagenetic. In particular, solution-enhancement by dissolution of rudist grains (RLA) and *Lithocodium-Bacinella* (BLA), cementation of some rudist grainstones and widespread matrix neomorphism of the RLA and OLA are particularly important, especially in proximity to the TSU. Permeability increases within the uppermost part of the Shuaiba Formation (Figure 10) as a result of more solution enhancement and lower volumes of pore occluding cementation than lower in the formation. This trend has been widely ascribed to solution leaching by meteoric water during emergence of the Shuaiba Formation in the late Aptian (e.g. Warrlich et al., 2010; Deville de Periere et al., 2011). Paragenetic relationships in this study, however, particularly with respect to dissolution around fractures and stylolites (e.g. Figure 7c), indicate that burial diagenesis was also an important control on pore enlargement. This might also have led to corrosion and rounding of micrite particles (e.g. Figure 8b). Similar features were described by Lambert *et al.* (2006) in the Mishrif Formation, and ascribed to solution-leaching prior to hydrocarbon emplacement, although Kaczmarek et al. (2015) have shown that imaging these particles at high magnification reveals that they can be polyhedral, not corroded, crystals. Regardless of the mechanisms, it is clear that the pore size and topology is most likely controlled by diagenetic modification that is specifically related to the skeletal composition of the facies association and depth beneath the Shuaiba – Nahr Umr unconformity.

Pore size and topology

The samples that were analysed as part of this study are typical of many Cretaceous reservoirs on the Arabian Plate in that they exhibit a wide range of pore sizes, often forming a complex network of sub-micron to centimetre scale pores, but with a dominance of meso- and micropores (eg. Budd, 1989, Moshier, 1989, Lambert et al., 2006, Volery, 2009, Hollis *et al.*, 2010; Deville de Periere *et al.*, 2011). In this study, more than 70% of the total pore volume is typically within pores that are < 1 μm diameter. A similar observation was made for the Natih Formation by Hollis *et al.* (2010).

The importance of micropore texture on porosity and permeability has been evaluated by Lambert et al. (2006) and Kaczmarek et al. (2015), who suggest that the most effective micropores form between subhedral micrite particles. There is little published data on the topology of meso- and micropores (e.g. Norbistrath et al., 2015), and so this study provides an important step in assessing pore topological

heterogeneity. Mesopores are also mostly flattened, although aspect ratios are slightly lower (~ 1.81) than micropores (> 1.87 ; Figure 13), particularly where biomouldic porosity is more abundant (1.67 and 1.73 in sample G1, Custom Bay and Xradia XCT respectively). Average mesopore co-ordination number is < 3 in all samples, consistent with the average co-ordination number of 2.84 reported by Jivkov et al. (2013). Co-ordination number is lowest where pores are more spherical (e.g. G1, where aspect ratio = 1.67 and co-ordination number is 1.08 based on Custom Bay data) as might be expected, since the pore shape will not facilitate interpore connectivity. Finally, a key observation is that the aspect ratio and co-ordination number of micropores is higher than for mesopores such that tortuosity is lower (< 6) than where a wider range of pore sizes is measured (eg. on the Custom Bay; Figure 13h).

Implications to permeability prediction

This study supports the conclusion of Archilla et al (2016) that knowledge of pore topological parameters can substantially improve prediction of permeability from total porosity. With the exception of total porosity, no single parameter improves or degrades permeability, but a combination of factors are important. It is striking that, in this dataset, the highest permeability (34.5 mD) was measured in the sample with the highest abundance of mesopores, highest aspect ratio and highest co-ordination number but the smallest dominant pore size (sample L1). The lowest permeability sample M1 (OLA, $K_h = 5.2$ mD), is fairly unremarkable in its pore topological parameters- it does not have the lowest dominant pore size, highest unresolved pore volume, highest specific surface area or tortuosity. What it lacks, however, is a network of meso- or macropores; only 3% of the pore volume is $> 1 \mu\text{m}$ (Table 3). By comparison, 9% of the total pore volume is $> 1 \mu\text{m}$ in sample G1 (RLA; $K_h = 13.9$ mD), but this includes well connected, large (mm – scale) macropores. In fact, the permeability of sample G1 is lower than might be expected from petrographical and core observations (Figure 4c), implying that a core plug does not provide a representative elemental volume for measurement of permeability on this type of facies. Certainly, the RLA in general has better reservoir quality than any other facies within the Shuaiba Formation (Figure 9). Consequently, the restriction of sample size to $< 1\text{mm}$ for X-ray CT analysis further limits our ability to measure the size and shape of the largest, flow-controlling pores in this facies association.

It has been shown that average co-ordination number increases as sample resolution increases. This could reflect better connectivity between micropores than meso- and macropores, but it could also simply reflect improved resolution of pore throats at higher magnification. Pore throat radii in most samples are $< 1 \mu\text{m}$ (Figure 12), indicating that pore to pore throat ratio is high in samples with higher volumes of meso- and macropores, and lower in microporous samples. This most likely contributes to the lower calculated tortuosity in the micropore, compared to the mesopore, network. In summary, the highest measured permeability in this sample set is within the sample with the highest volume of

mesopores, but where larger (mm to cm scale) biomoulds are present, within the RLA, actual permeabilities are likely to be higher.

Implications to reservoir recovery

In general, flatter pores and high co-ordination number reduces tortuosity, and should therefore facilitate better recovery efficiency. The importance of pore scale heterogeneity should also not be forgotten, however. Hollis et al. (2010) highlighted the importance of pore heterogeneity, with respect to pore size, connectivity and shape, on recovery efficiency. In particular, they showed that samples with the highest permeability can also have the highest residual oil saturation after imbibition because flow occurs preferentially via the largest pores, bypassing smaller pores. In this study, samples of the RLA (G1) and the BLA (eg. M2) have moderate permeability but exhibit a highly heterogeneous pore network with a wide range of pore sizes (Figure 12). In the case of sample G1, the largest pores were not captured by X-ray CT analysis. In these cases, it would be expected that recovery would be dominated by production from macropores, with the potential to bypass high volumes of hydrocarbon within the dominant micropore network (>90% of the total pore volume). Conversely, in sample L1, a well-connected network of meso- to micropore should result in a more even sweep. Similarly, although sample M1 has a poor permeability, the network of well-connected micropores could also facilitate more efficient recovery than in the higher permeability, more heterogeneous samples such as G1 and M2.

CONCLUSIONS

This study provides one of the first, comprehensive pore topological datasets for a range of reservoir rock types on different scales within a single carbonate reservoir across multiple fields. Through the integration of 2D and 3D observations and quantitative characterization of pore shape and size it is possible to draw a series of conclusions which could have far-reaching implications to our understanding of static reservoir properties and reservoir recovery in carbonate reservoirs. In particular:

- Although there is not a strong relationship between lithofacies association and reservoir quality, the diagenetic overprint appears to have been influenced by primary rock texture and composition, as well as depth beneath the TSU. The best reservoir quality is found within the RLA, which solution enhancement of biomoulds (after rudists), fractures and primary interparticle macropores has created a well-connected macropore system. The large size of these pores means that they are not always captured by routine core analysis plugs or X-ray CT analysis, as they might have a representative elemental volume that is larger than a standard core analysis plug.

- Within the Shuaiba Formation, over 70% of the pore network is contained within pores that are $< 1 \mu\text{m}$ diameter (ie. microporosity). Although these pores are hard to image, they will offer the largest volume for hydrocarbon storage with these reservoirs. The small pore size suppresses permeability, but relatively homogenous, flattened aspect ratios facilitate connectivity and might support a relatively efficient sweep in the absence of larger, cross-cutting, connected macropores.
- The highest permeability within the sample set occurs in sample L1, which has the highest volume of mesoporosity, most 3D equivalent pore radii $>10 \mu\text{m}$, the highest aspect ratio and highest co-ordination number.
- Permeability is apparently controlled by pore size, shape and co-ordination number. The highest permeability, and lowest tortuosity, occurs in samples with well-connected meso- and macropores, high aspect ratios, mean co-ordination number > 2 and the lowest specific surface area.
- Although the RLA and BLA facies associations have the best overall porosity and permeability, they also have the most heterogeneous pore network with respect to pore size distribution, pore throat radii and pore shape. Consequently, it would be expected the sweep efficiency in these samples would be poorer than from more homogeneous, finer grained lithofacies associations (OLA and BFLA), resulting in higher volumes of bypassed oil and residual oil saturation.

ACKNOWLEDGEMENTS

We gratefully acknowledge Petroleum Development Oman and the Ministry of Oil and Gas for supporting this project and for permission to publish. We are grateful to the Manchester X-ray Imaging Facility for supporting this study; this work was also made possible by the facilities and support provided by the Research Complex at Harwell, funded in part by the EPSRC (EP/I02249X/1)

REFERENCES

- Ahr, W., 2008, *Geology of Carbonate Reservoirs*. Published John Wiley & Sons Inc., 277pp
- Al Furqani, S., 2008. *Diagenesis of The Upper Shuaiba Reservoir in The Malaan Field, Northern Oman*. Unpublished MS thesis, Sultan Qaboos University, Muscat.
- Al Hajri, A., 2015. *Timing reservoir quality enhancement at the Shuaiba/Nahr Umr boundary, Oman*. Unpublished PhD thesis, University of Manchester

Al Sharhan, A.S., 1987. Petrography and Stable Isotope Composition of Baroque Dolomite From The Shuaiba Formation (Lower Cretaceous), Abu Dhabi, United Arab Emirates. *Journal of African Earth Sciences*, 6(6), pp.881-890.

Amthor, J., Kerans, C and Gauthier, P., 2010, Reservoir characterisation of a Shuaiba carbonate ramp-margin field, northern Oman. *GeoArabia Special Publication*, 4, v.2, 549-576

Anselmetti, F., Luthi, S and Eberli, G., 1998. Quantitative characterization of carbonate pore systems by digital image analysis. *AAPG Bulletin*, 83, 1815-1836

Archilha, N., Missagia, R., Hollis, C., de Ceia, M., McDonald, S., Lima Neto, I., Eastwood, D and Lee, P., 2016. Permeability and acoustic velocity controlling factors determined from X-ray tomography images of carbonate rocks. *AAPG Bulletin*, 100, 1289-1309

Borgomano, J., Masse, J.P., and Al Maskiry, S., 2002. The Lower Aptian Shuaiba Carbonate Outcrops in Jebel Akhdar, Northern Oman: Impact on Static Modelling for Shuaiba Petroleum Reservoirs. *AAPG Bulletin*, 86(9), pp.1513–1529

Budd, D., 1989. Micro-Rhombic Calcite and Microporosity in Limestones: A geochemical Study of The Lower Cretaceous Thamama Group, U.A.E. *Sedimentary Geology*, 63, 293-311.

Choquette, P.W., and Pray, L.C., 1970. Geologic Nomenclature and Classification of Porosity in Sedimentary Carbonates: *AAPG Bulletin*, 54(2), pp.207-244.

de Periere, M.D., Durlot, C., Vennin, E., Lambert, L., Bourillot, R., Caline, B., Poli, E., 2011. Morphometry of Micrite Particles in Cretaceous Microporous Limestones of The Middle East: Influence on Reservoir Properties. *Marine and Petroleum Geology*, 28, 1727-1750

Droste, H and van Steenwinkel., M., 2004. Stratal geometries and patterns of platform carbonates: the Cretaceous of Oman. In: *Seismic imaging of carbonate reservoirs and systems* (Ed G. Eberli, J-L Masseferro and J.F.R Sarg). *AAPG Memoir* 81, 185-206

Droste, 2010, Sequence stratigraphic framework of the Aptian Shuaiba Formation in the Sultanate of Oman, *GeoArabia Special Publication*, 4, v.1, 229-283

Flügel, E. 2004. *Microfacies of Carbonate rocks: Analysis, Interpretation and Application*. New York, Springer.

Forbes, G. A., Jansen, H.S.M. and Schreurs, J., 2010. *Lexicon of Oman Subsurface Stratigraphy*. Manama, Gulf PetroLink

Hillgartner, H., 2010, Anatomy of a microbially constructed, high-energy, ocean facing carbonate platform margin (earliest Aptian, north Oman Mountains). *GeoArabia Special Publication*, 4, v.1, 285-300

Hollis, C., Vahrenkamp, V., Tull, S., Mookerjee, A., Taberner, C., Huang, Y., 2010. Pore System Characterisation in Heterogeneous Carbonates: An alternative Approach to Widely-used Rock-typing Methodologies. *Marine and Petroleum Geology*, 27(4), 772–793.

Immenhauser, A., Van Der Kooij, B., Van Vliet, A., Schlager, W., and Scott, R. W., 2001. An Ocean-Facing Aptian-Albian Carbonate Margin, Oman. *Sedimentology* 48: 1187-1207.

Immenhauser, A. and Scott, R.W., 2002. An Estimate of Albian Sea-level Amplitudes and its Implication for the Duration of Stratigraphic Hiatuses. *Sedimentary Geology*, 152, pp.19–28.

Immenhauser, A and Rameil, N., 2012. Interpretation of ancient epikarst features in carbonate successions- a note of caution. *Sedimentology*.

Immenhauser, A., Hillgartner, H., Sattler, U., Bertotti, G. Schoepfer, P., Homewood, P., Vahrenkamp, V., Steuber, T., Masse, J.-P., Droste, H., Taal-van Koppen, J., van der Kooij, B., van Bentum, E., Verwer, K., Hoogerduijn Strating, E., Swinkels, W., Peters, J., Immenhauser-Potthast, I. and Al Maskery, S., 2004. Barremian-lower Aptian Qishn Formation, Haushi-Huqf area, Oman, a new outcrop analogue for the Kharaiib/Shu'aiba reservoirs. *GeoArabia*, 9, 153–194

Kaczmarek, S., Fullmer, S and Hasiuk, F., 2015. A universal classification scheme for the microcrystals that host limestone microporosity. *Journal of Sedimentary Research*, 85, 1197-1212

Lambert, L., Durllet, C., Loreau, J.P., Marnier, G., 2006. Burial Dissolution of Micrite in Middle East Carbonate Reservoirs (Jurassic–Cretaceous): Keys For Recognition and Timing. *Marine and Petroleum Geology*, 23, pp.79–92.

Lonoy, A., 2006, Making sense of carbonate pore systems. *AAPG Bulletin*, 90, 1381-1405

Lucia, J and Loucks, R., 2013. Micropores in carbonate mud: early development and petrophysics. *GCAGS Journal*, 2, 1-10

Lucia, J., 2007. Carbonate reservoir characterisation. Springer-Verlag, New York. 225pp, 2nd edition

Malchus, N., 1998. Aptian (Lower Cretaceous) Rudist Bivalves from NE Spain: Taxonomic Problems and Preliminary Results. *Memoire special*, 22, pp.181-191.

Masse, J. P., Borgomano, J. and Al Maskiry, S., 1998. Stratigraphy and tectonosedimentary evolution of a late Aptian-Albian carbonate margin: the northeastern Jebel Akhdar (Sultanate of Oman). *Sedimentary Geology*, 113: 269-280.

Moshier, S., 1989. Development of Microporosity in A micritic Limestone Reservoir, Lower Cretaceous, Middle East. *Sedimentary Geology*, 63, pp.217-240

Norbisrath, J., Eberli, G., Laurich, B., Desbois, G., Weger, R., Urai, J., 2015. Electrical and fluid flow properties of carbonate microporosity types from multiscale digital image analysis and mercury injection. *AAPG Bulletin*, 99, 2077-2098

Pittet, B., Buchem, F.S.P, Hillgärtner, H., Razin, P., Groätsch, J. and Droste, H., 2002. Ecological Succession, Palaeoenvironmental Change, and Depositional Sequences of Barremian–Aptian Shallow-Water Carbonates in Northern Oman. *Sedimentology*, 49, pp.555-581.

Rameil, N., Immenhauser, A., Warrlich, G., Hillgarner, H and Droste, H., 2010. Morphological patterns of Aptian Lithocodium-Bacinella geobodies: relation to environment and scale. *Sedimentology*, 57, 883-911

Raspini, A., 1998. Microfacies Analysis of Shallow Water Carbonates and Evidence of Hierarchically Organized Cycles: Aptian of Monte Tobenna, Southern Apennines, Italy. *Cretaceous Research*, 19, pp.197-223.

Schroeder, R., van Buchem, F, Cherchi, a, Baghbani, D, Vincent, B, Immenhauser, A and Granier, B., 2010. Revised orbitolinid biostratigraphic zonation for the Berremian-Aptian of the eastern Arabian Plate and implications for regional stratigraphic correlations. *GeoArabia Special Publication*, 4, v.1, 49-96

Van Buchem, F., Hillgärtner, H. Grötsch, G., Al Mansouri, A., Billing, I., Droste, H, Oterdoom, W. and Steenwinkel, M., 2002. High-resolution Sequence Stratigraphic Architecture of Barremian/Aptian Carbonate Systems in Northern Oman and the United Arab Emirates (Kharaiib and Shu'aiba Formations). *GeoArabia* 7(3): 461-500.

Van Buchem, F., Al-Husseini, M., Maurer, F., Droste, H., Yose, L. A., 2010. Sequence-stratigraphic synthesis of the Barremian – Aptian of the Eastern Arabian Plate and Implications for the Petroleum Habit. *GeoArabia Special Publication*, 4, v.1, 9-48

Vilas, L., Masse, J.P., and Arias, C., 1995. Orbitolina Episodes in Carbonate Platform Evolution: The Early Aptian Model From SE Spain. *Palaeogeography, Palaeoclimatology, Palaeoecology*, 119, pp.34-45.

Warrlich, G., Rameil, N., Gittins, J., Mahruqi, I., Johnson, T., Alexander, D., Wassing, B., van Steenwinkel, M and Droste, H, 2010. Reservoir characterisation of data-poor fields with regional analogues: A case study from the Lower Shu'aiba in the Sultanate of Oman. *GeoArabia Special Publication* 4 v.2., 577-6042: 577-604.

Weger, R., Eberli, G., Baechle, G, Massaferro, J and Sun, Y-F., 2009. Quantification of pore structure and its effect on sonic velocity and permeability in carbonates. AAPG Bulletin, 93, 1297-1317

Figures and Tables

Figure 1a) Stratigraphic column for the lower Cretaceous, showing the position of the Shuaiba and Nahr Umr Formations and the location of the top Shuaiba unconformity. B) Map showing the location of the study area and the palaeo-depositional environment during late Aptian, (Immenhauser et al, 2004; van Buchem et al., 2010, modified)

Figure 2 a) Sketch showing the sequence stratigraphic model for the Shuaiba Formation in the studied modified after Droste, (2004) b) Modal analysis shows higher volume of cement in grain-dominated lithofacies (i.e. Rudist-dominated lithofacies) than the mud dominated lithofacies (i.e. Bacinella and Orbitolina-dominated lithofacies)

Figure 3: X-ray CT image processing, based on Custom Bay data

Figure 4 Facies in core & thin section a) Contact between Nahr Umr formation (NU) and Shuaiba Formation (SF), showing dark green-grey mudstone (MLA) within the Nahr Umr Formation b) benthic foraminiferal wackstone (BFLA) in well L1 c) Rudist floatstone in well G1, with rudists and biomoulds after rudists arrowed), d) fragmented rudist (r) with mudstone matrix (m) and solution-enhanced fracture (arrowed) e) Laminar Lithocodium Bacinella (LB) packstone f) Lithocodium/Bacinella (arrowed), with cemented intraparticle macropores g) Orbitolina wack-packstone h) conical Orbitolina (arrowed)

Figure 5a) drusy calcite cemented fracture (f), biomoulds (b) and interparticle macropore (arrowed) in rudist floatstone, b) cemented interparticle macropores in Orbitolina packstone, where intraparticle macropores in Orbitolina remains open (arrowed) c) cemented fracture (f) and biomoulds (b) in rudist floatstone

Figure 6 Volume of cement, replacive spar and macropores, with variation by depth beneath the Shuaiba-Nahr Umr unconformity, per lithofacies association

Figure 7a) solution enhanced interparticle macropores in rudist grainstone (arrowed) b) intraparticle macropores within Lithocodium/Bacinella (arrowed) c) solution-enhanced fracture in rudist floatstone (f). Note that corrosion of pore filling cements (arrowed) indicates that dissolution postdates calcite cementation d) pelmouldic micropores (p) in rudist peloidal pack-grainstone, with cemented interparticle macropores (arrowed) Table 1 Summary of analytical conditions for X-ray CT analysis

Figure 8 Micropores as viewed by ESEM. A) interparticle micropores in sample M1, b) solution enhanced fracture (A) with apparent solution-modified micropores in peloid adjacent to fracture (arrowed, with peloid outlined by dotted line) in sample G1 c) sample M2 and d) sample L1 show interparticle micropores in ESEM (upper) and binarized (lower) images. Tortuosity (τ) was measured

in each image as the ratio of the longest path of fluid flow (L_a) (red lines) to the shortest distance between the two points which represent the entry and the exist points of the fluid (L) (i.e. the end and the beginning of the red line).

Figure 9: Core analysis by well and by facies

Figure 10: Core analysis by depth and lithofacies per well

Figure 11: Thin section photomicrographs, processed X-ray CT images and extracted pores for samples G1 (a, X-radia XCT), M1 (b, X-radia XCT) and M2 (c, Custom Bay)

Figure 12 Comparison of pore size data from X-ray CT and ESEM analysis with pore throat size from MICP analysis. Unresolved porosity (%) is from Custom Bay X-ray CT analysis

Figure 13 Pore topological properties as determined by X-ray CT and image analysis of ESEM images

Figure 14 Covariation of average pore topological parameters (red= CustomBay, green= X-Radia XCT and blue= ESEM)

Table 1 Summary of analytical conditions for X-ray CT analysis

Table 2, Average, minimum and maximum volumes of macropores, cement and replacive spar based on modal analysis of 42 samples. All values are percentages

Table 3 Pore geometrical data obtained by X-ray CT analysis

Table 4 Pore geometrical data obtained by ESEM

Table 5 Multilinear regression to determine controls on permeability

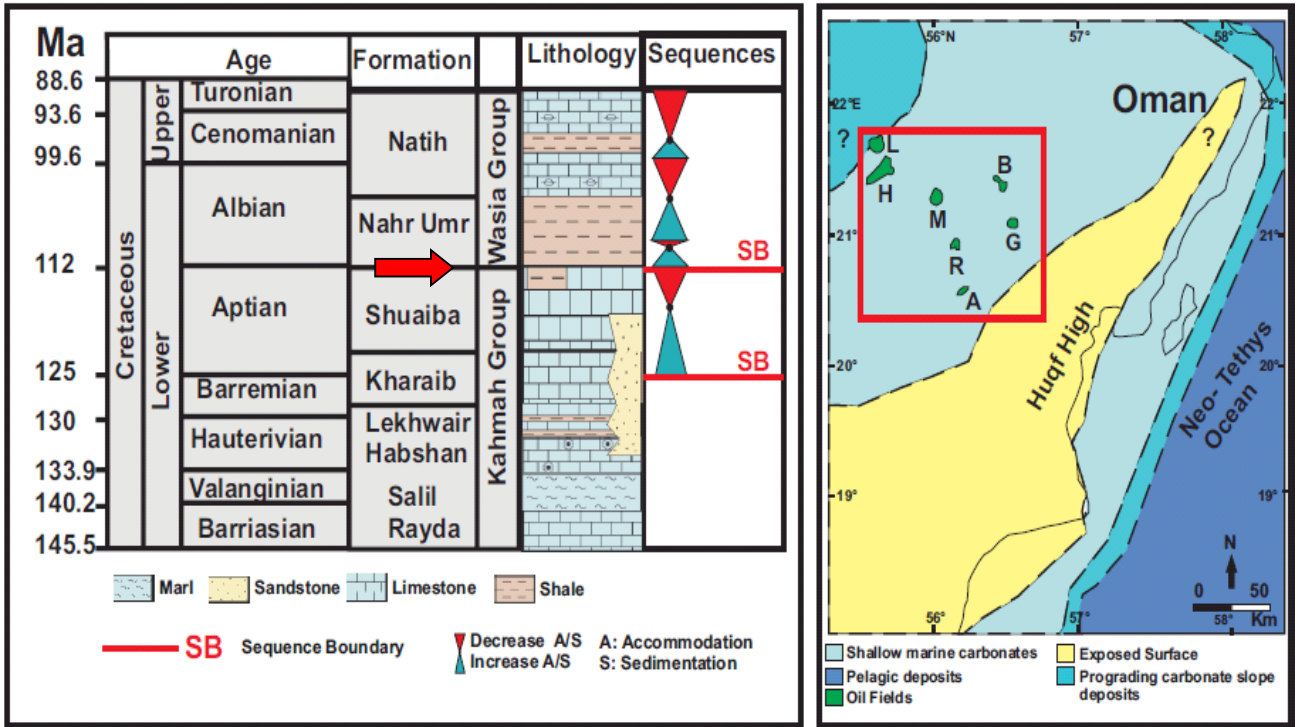


Figure 1

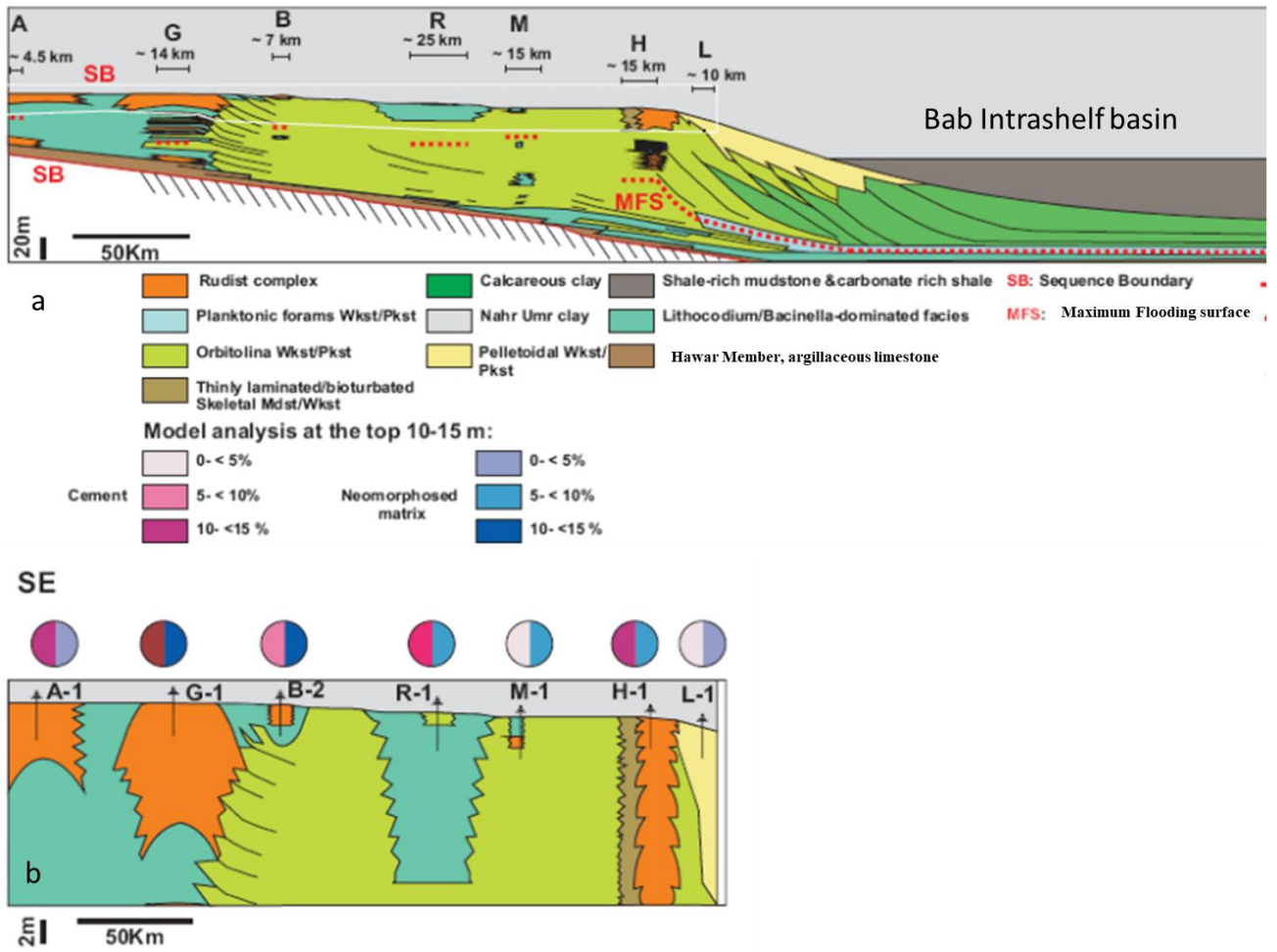


Figure 2

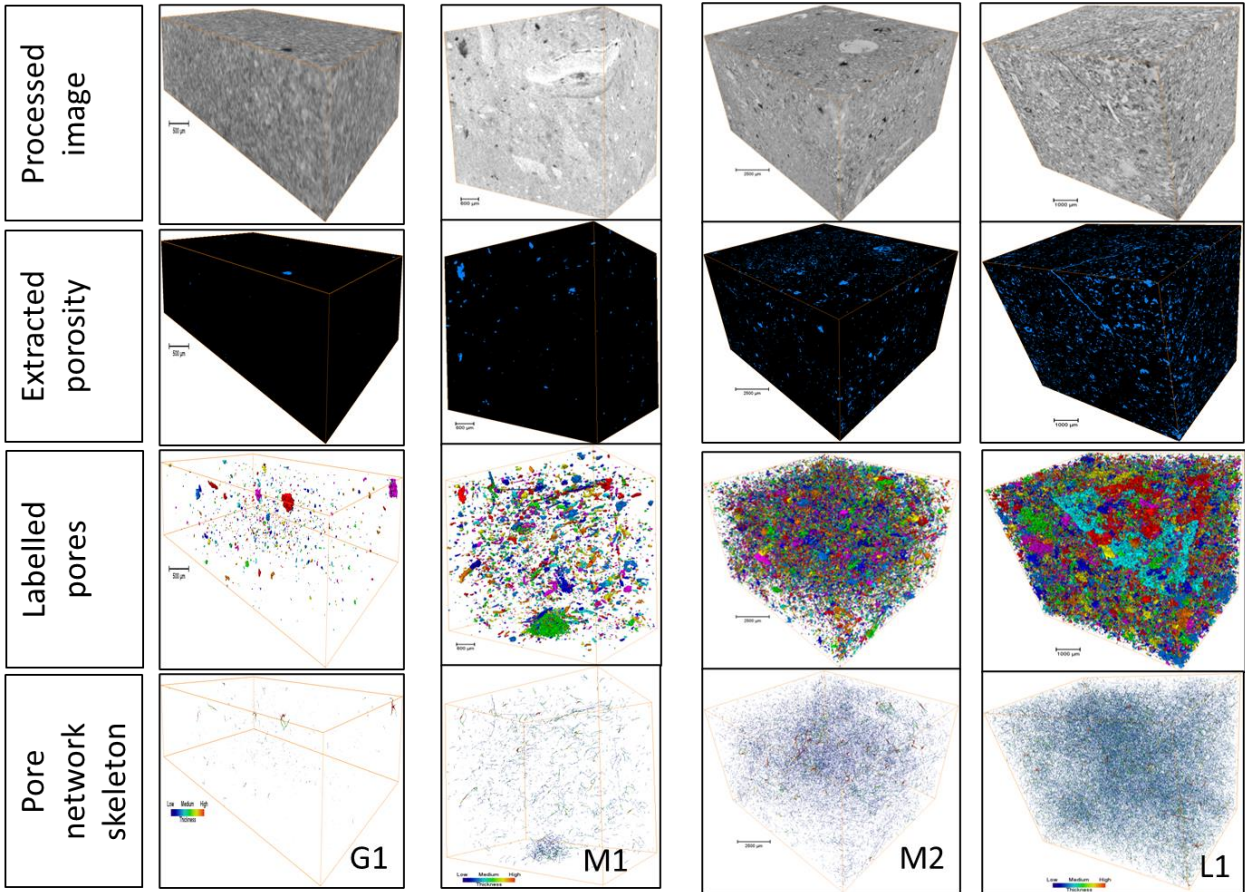


Figure 3

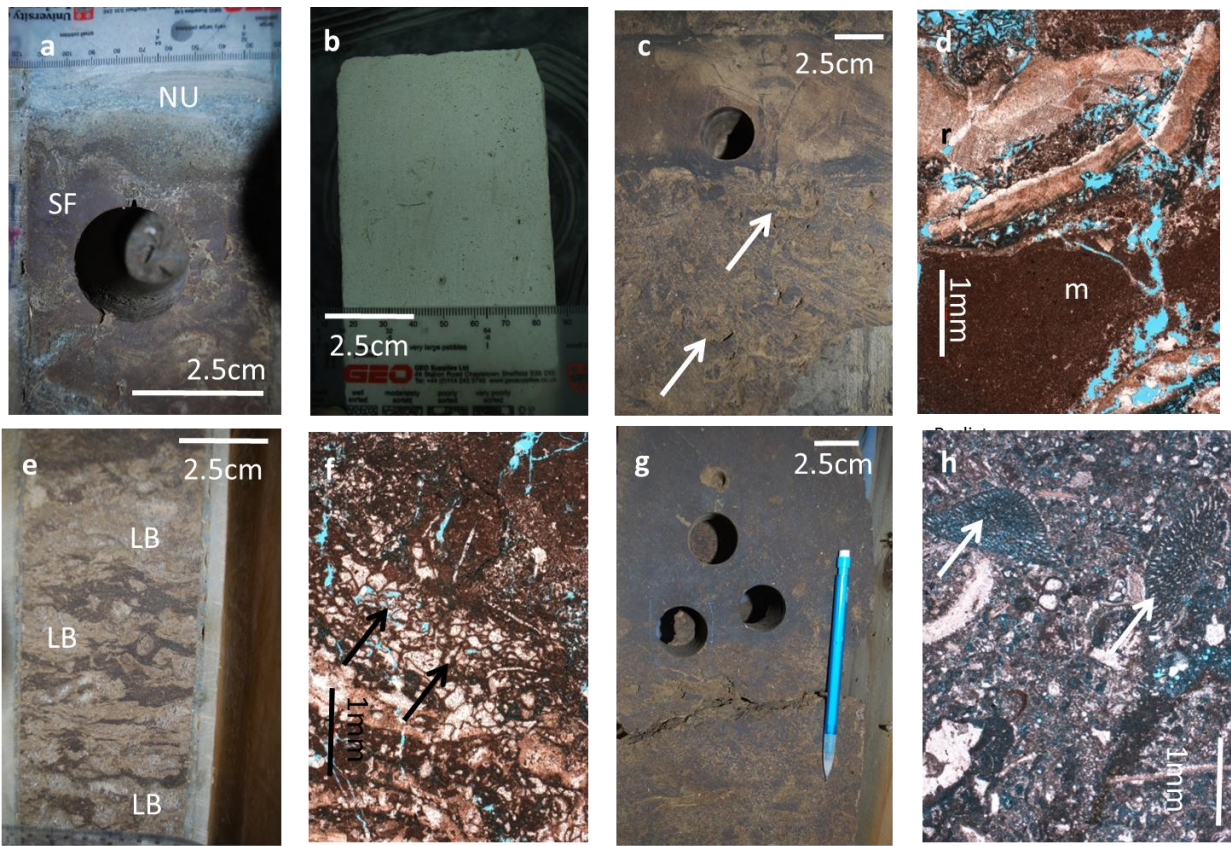


Figure 4

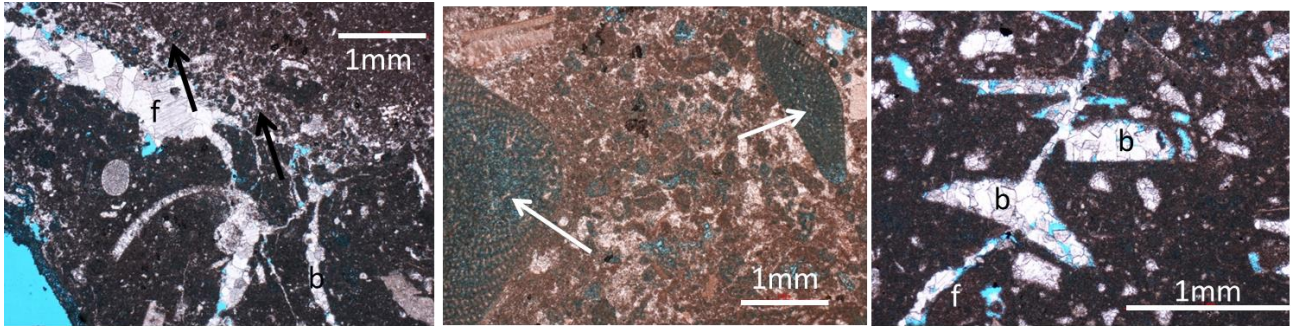


Figure 5

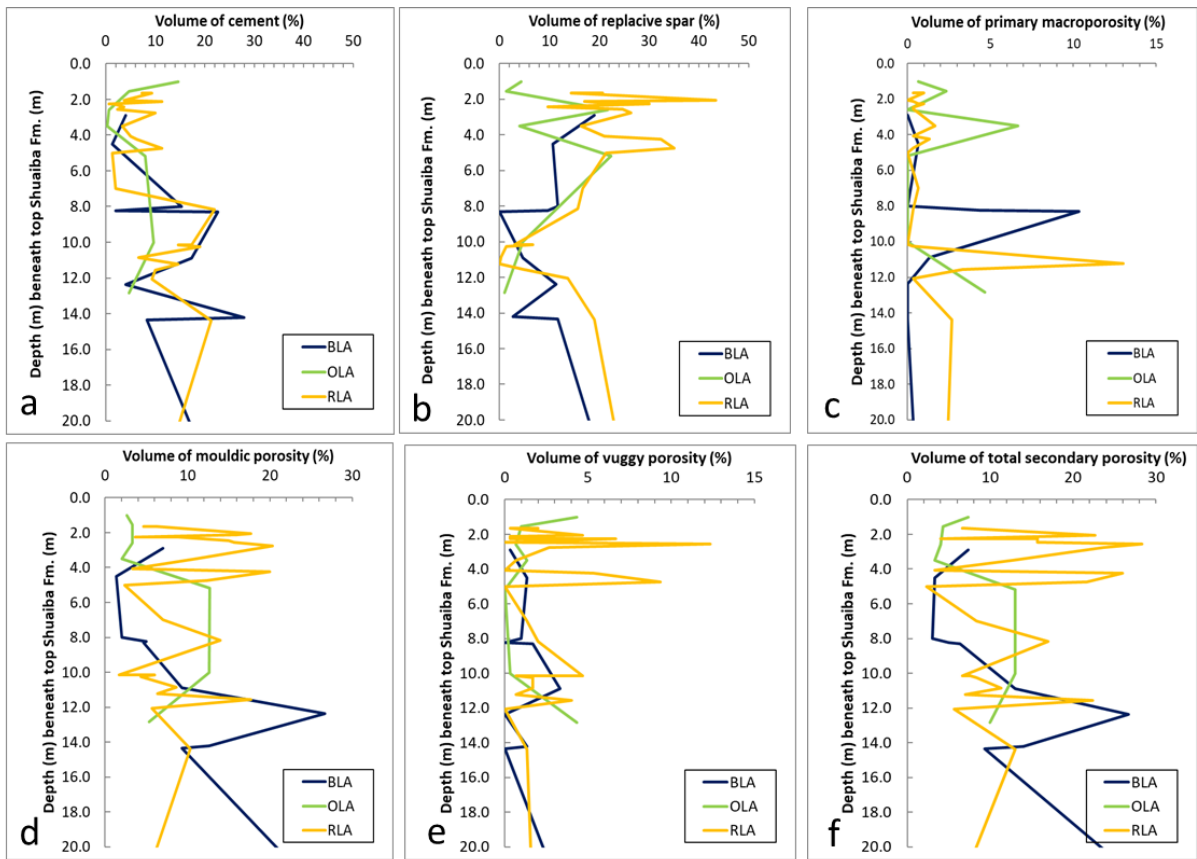


Figure 6

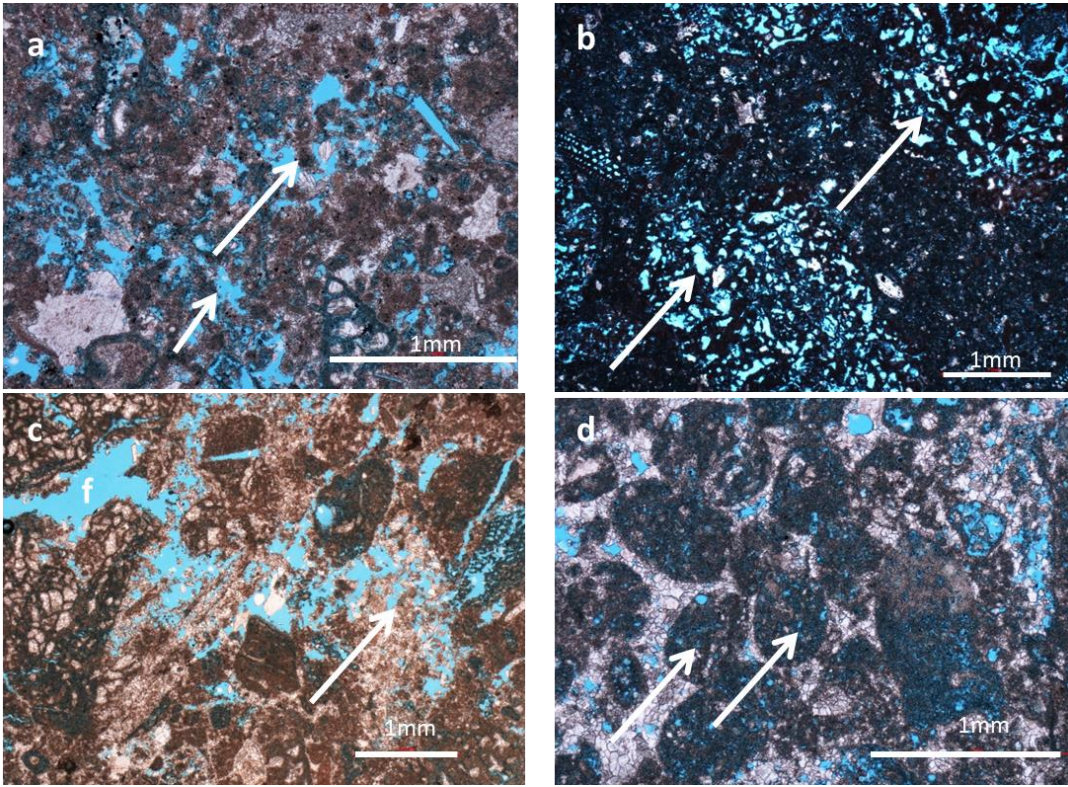


Figure 7

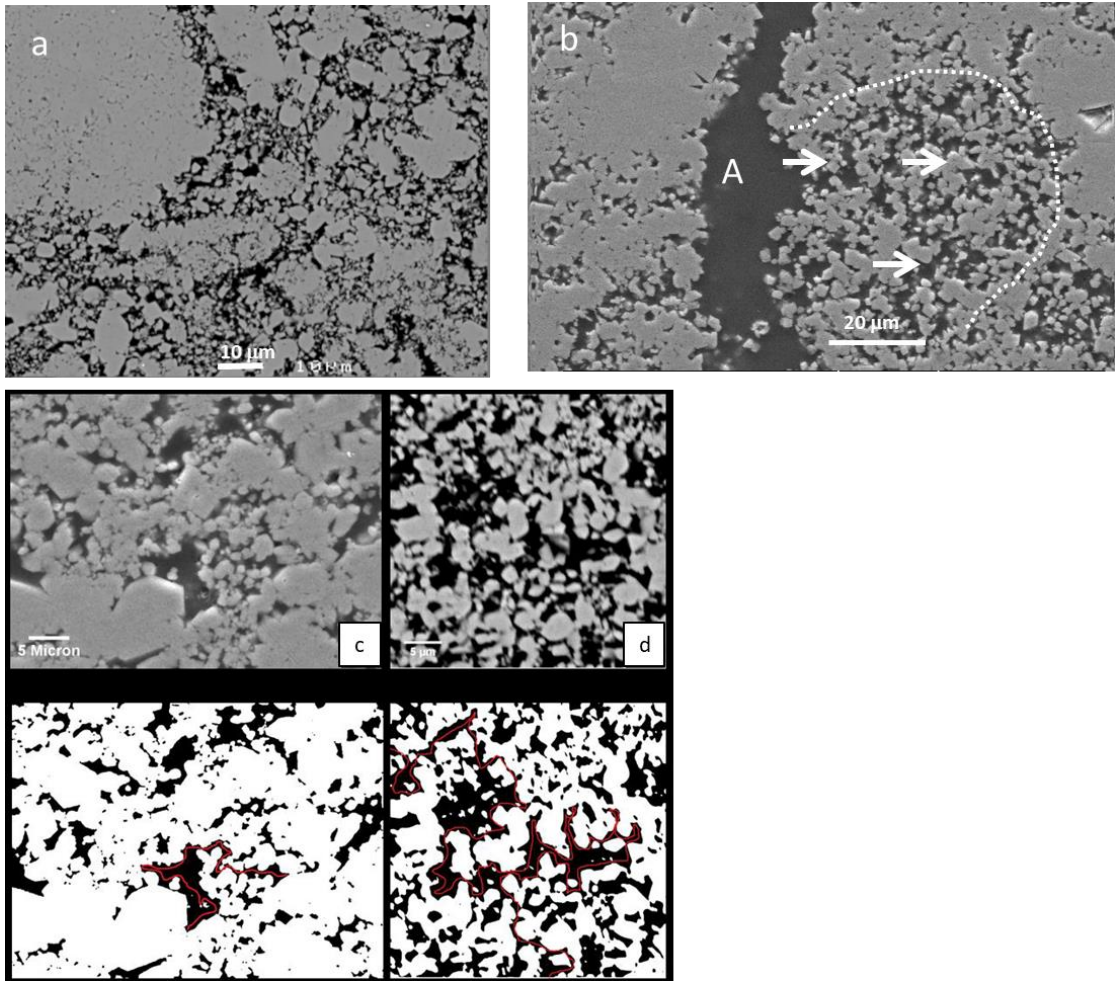


Figure 8

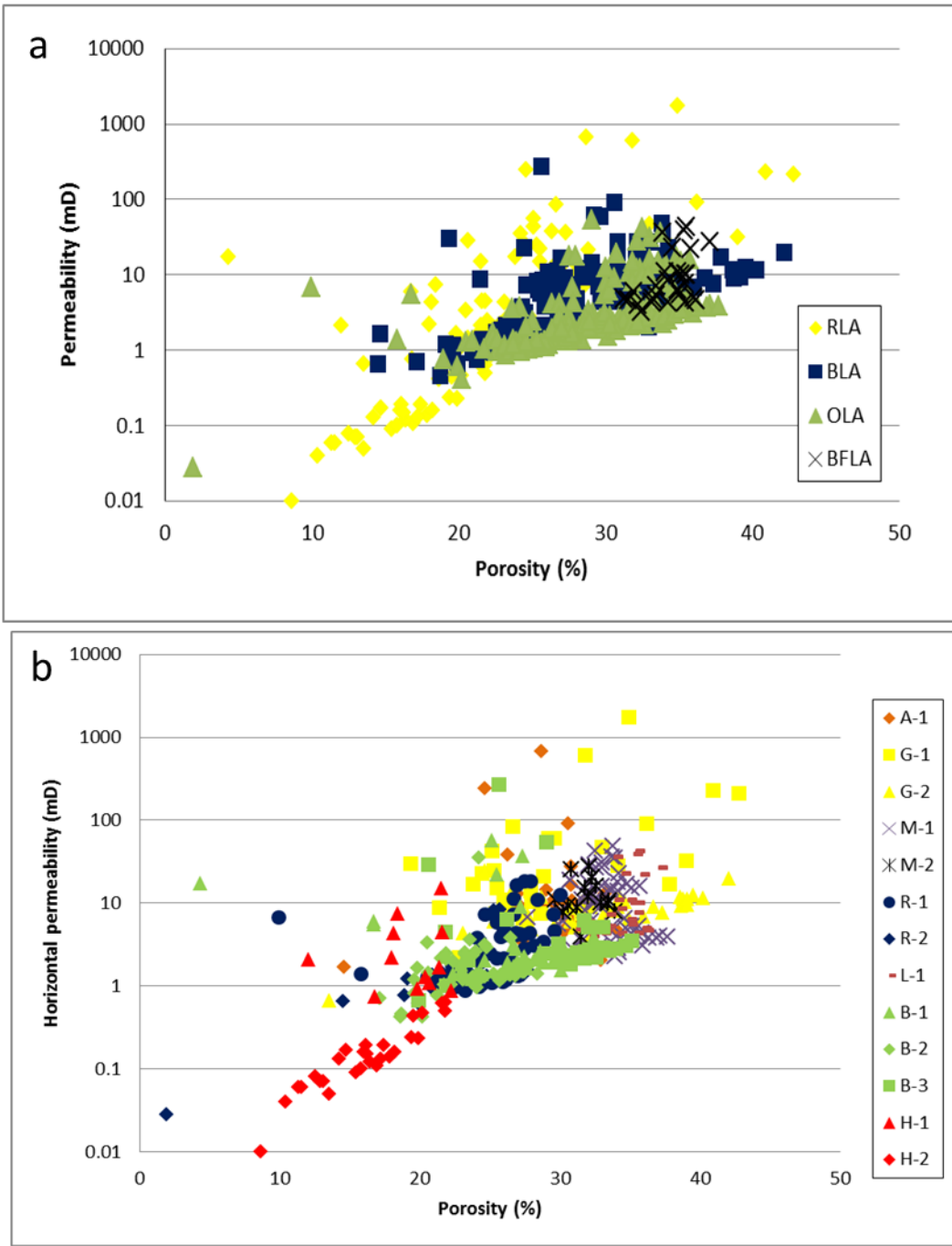


Figure 9

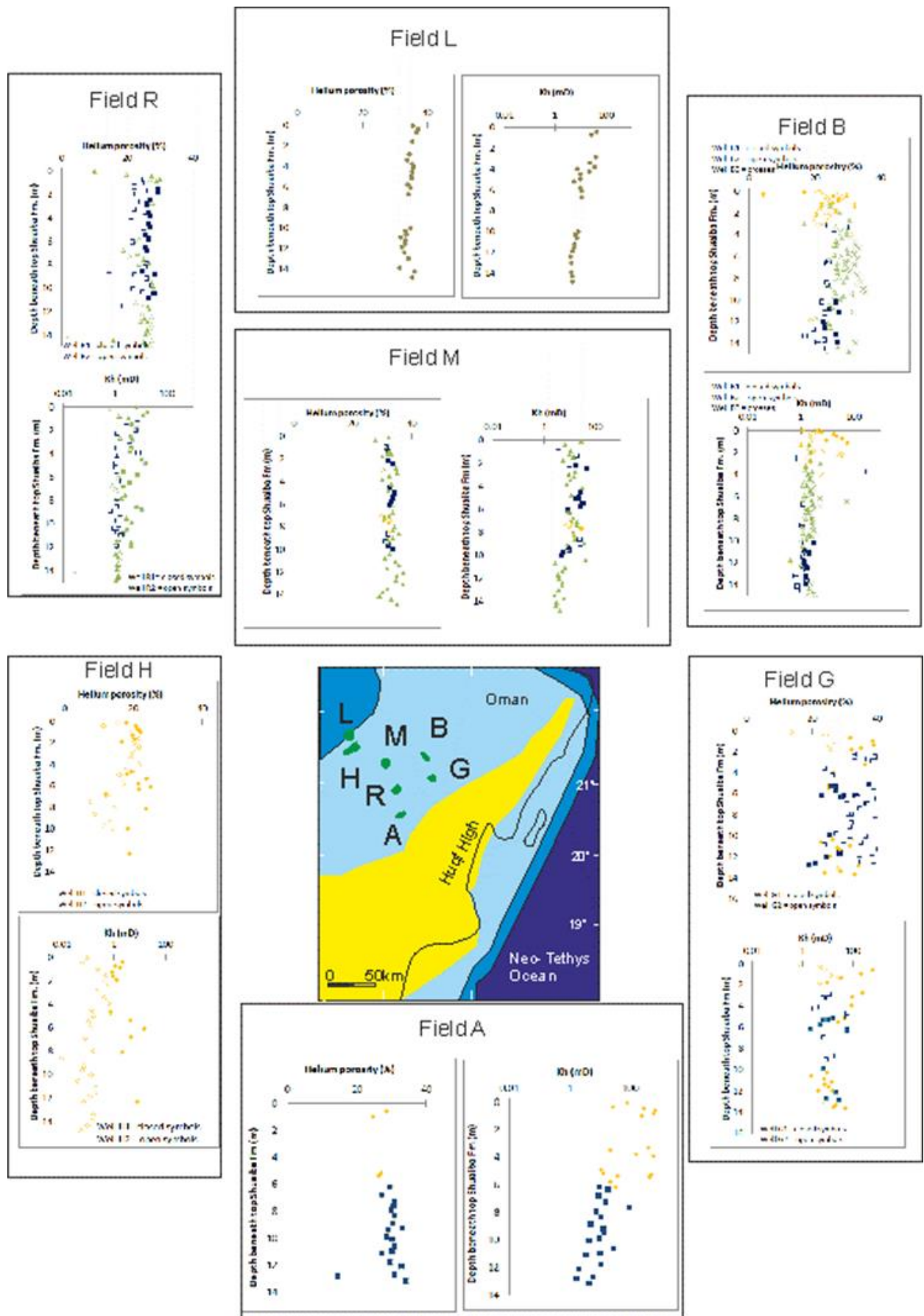


Figure 10

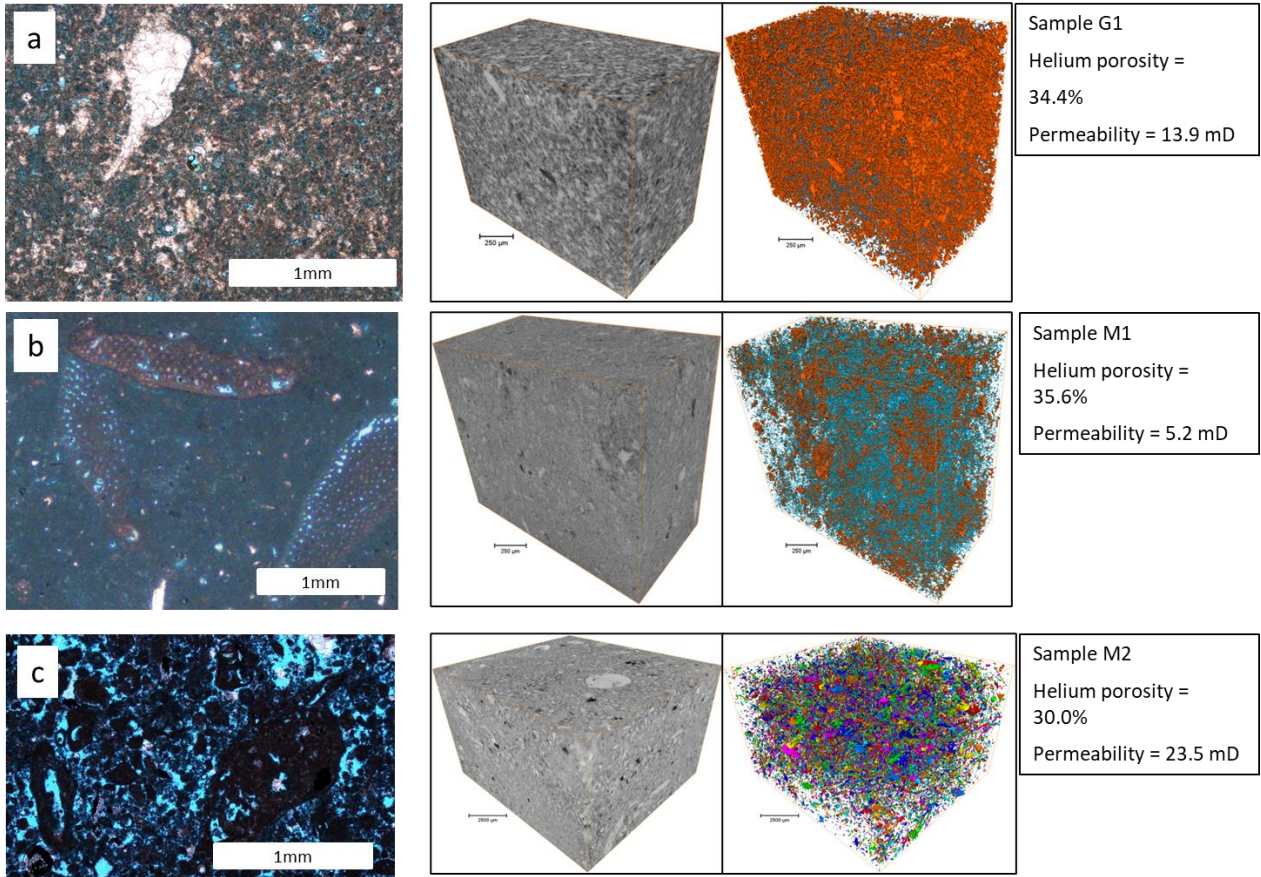
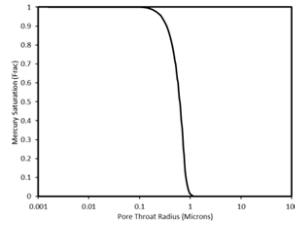
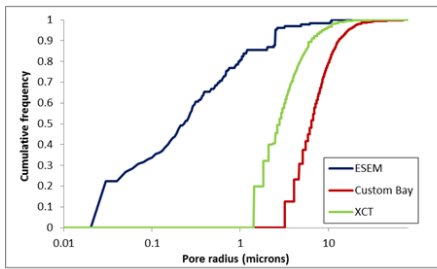
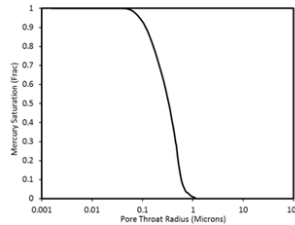
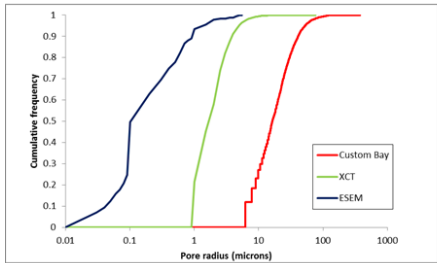


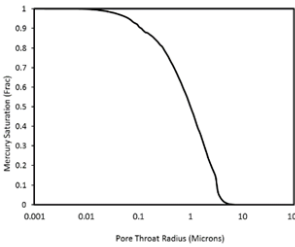
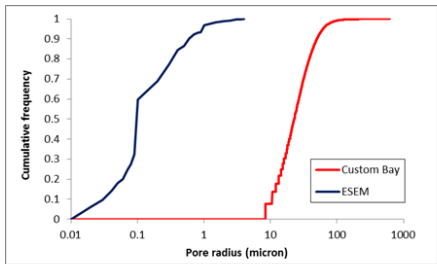
Figure 11



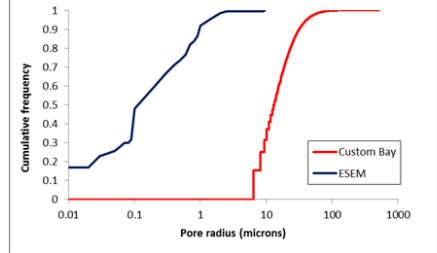
Sample G1
 Helium porosity = 34.4%
 Permeability = 13.9 mD
 Unresolved porosity = 99.8%



Sample M1
 Helium porosity = 35.6%
 Permeability = 5.2 mD
 Unresolved porosity = 97.4%



Sample M2
 Helium porosity = 30.0%
 Permeability = 23.5 mD
 Unresolved porosity = 91.5%



Sample L1
 Helium porosity = 23.0%
 Permeability = 34.5 mD
 Unresolved porosity = 69.9%

Figure 12

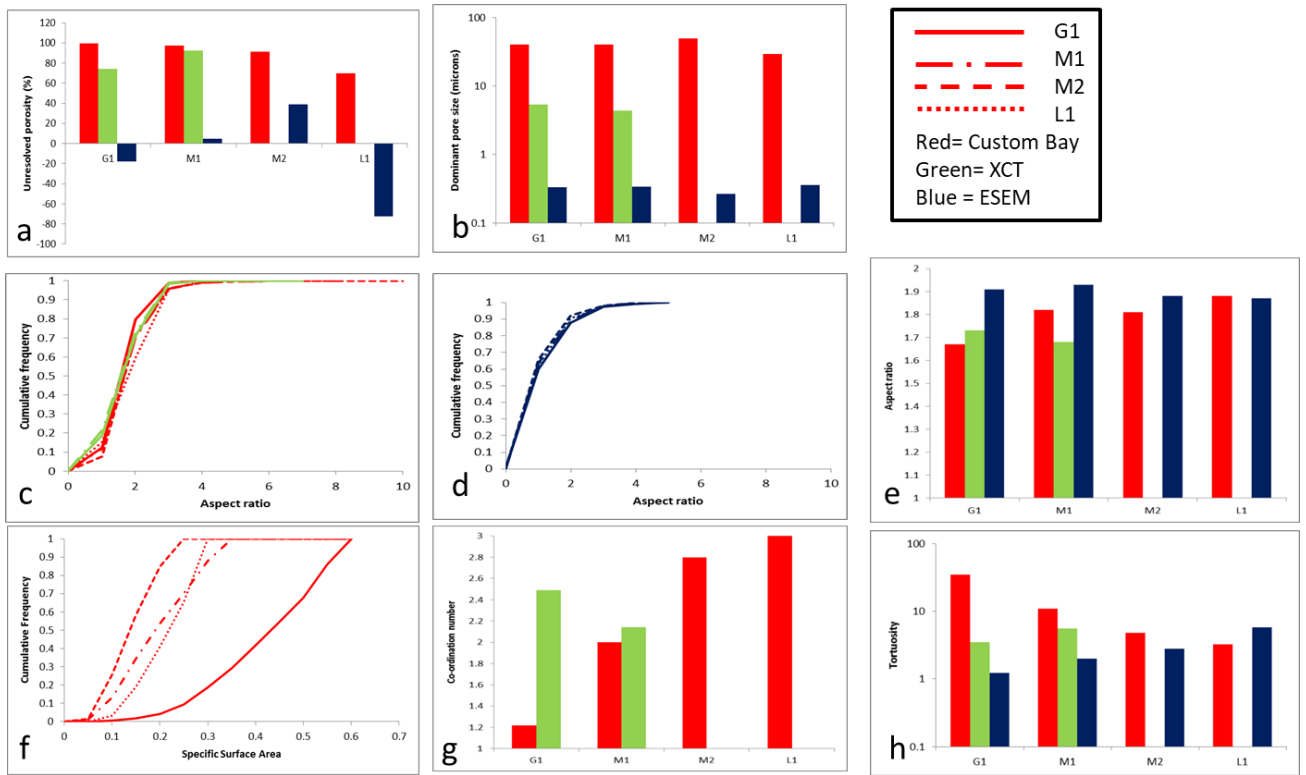


Figure 13

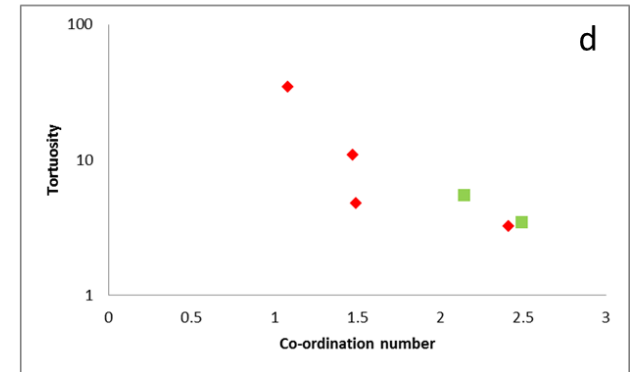
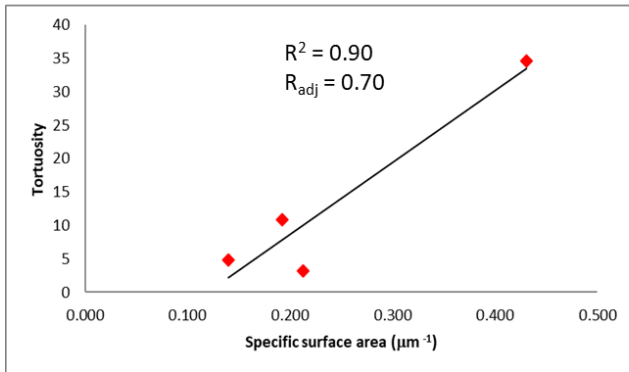
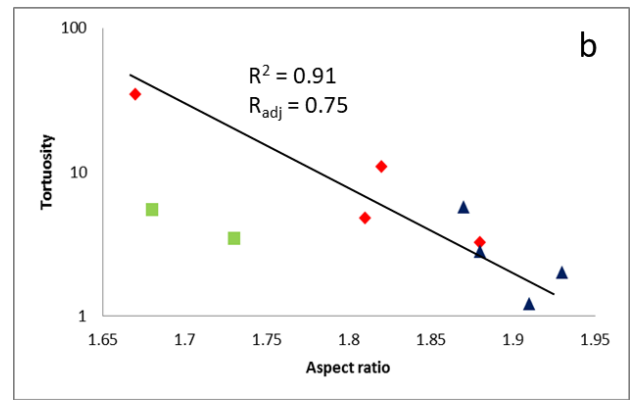
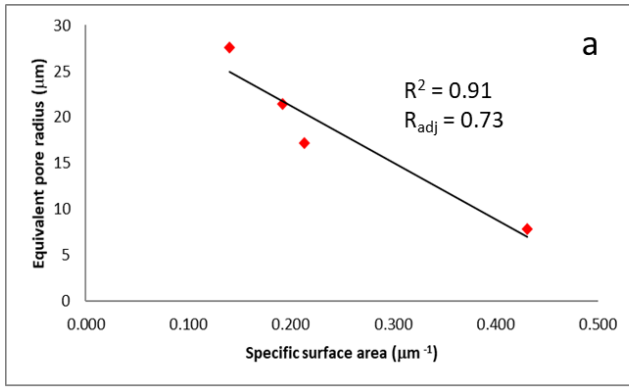


Figure 14

Well	Sample No.	Depth	LA	Depth beneath unconformity (m)	Scanner	Magnification	Exposure time (sec)	Acquisition time	Current (uA)	Energy (KeV)	Filter	Pixel Size (um)	No of Reconstructed images	No. Analysed images	Φ(%)	K (mD)	Pore type
								(Hr)									
G-1	G1	Skeletal wackestone	RLA	1.25	Micro-XRadia XCT	10x	15	18.5	166	60	2	2.36	1963	578	34.4	13.9	Primary interparticle macro- and microporosity and mouldic porosity
G-1	G1	Skeletal wackestone	RLA	1.25	Nikon Custom Bay	40x	0.71	0.15	108	134	No	5.2	1301	183			
M-1	M1	Orbitolina wackestone	OLA	11.35	Micro-XRadia XCT	10x	30	20.14	110	80		2.22	966	817	35.6	5.2	Intraparticle and interparticle primary micro- and macroporosity and mouldic porosity
M-1	M1	Orbitolina wackestone	OLA	11.35	Nikon Custom Bay	21x	0.71	0.18	108	134	No	10	1494	611			
M-2	M2	Skeletal wackestone to packstone	BLA	0.15	Nikon Custom Bay	15x	1	0.52	170	190	copper	13.5	630	594	30.0	23.5	Intraparticle and interparticle primary micro- and macroporosity and mouldic porosity
L-1	L1	Skeletal wackestone to packstone	BFLA	2.52	Nikon Custom Bay	20x	1	0.52	150	190	No	10.4	1690	701	23.0	34.5	Interparticle microporosity

Table 1 Summary of analytical conditions for X-ray CT analysis

		Total primary macroporosity	Total mouldic porosity	Total vuggy porosity	Other secondary macroporosity	Total secondary macroporosity	Total cement	Total replacive spar
Field A	Mean	0.70	9.70	0.70	0.59	11.00	9.89	15.11
	Min	0.00	2.33	0.00	0.00	2.33	1.33	6.67
	Max	2.67	16.00	2.00	1.33	16.99	22.00	21.33
Field B	Mean	0.29	9.92	0.37	0.08	10.38	6.54	16.21
	Min	0.00	3.34	0.00	0.00	3.34	0.67	4.67
	Max	1.00	26.67	2.00	0.33	26.67	9.67	23.67
Field G	Mean	2.51	11.02	3.82	0.41	15.25	12.63	15.47
	Min	0.00	1.67	0.67	0.00	2.99	1.67	0.00
	Max	13.00	21.00	12.33	2.33	28.33	28.00	43.33
Field M	Mean	3.92	3.92	1.58	0.08	5.58	1.92	9.08
	Min	0.00	2.00	0.00	0.00	3.34	0.33	1.00
	Max	6.67	5.33	4.33	0.33	10.00	4.67	21.67
Field R	Mean	1.22	2.44	2.22	0.33	5.00	6.89	5.44
	Min	0.67	1.33	1.00	0.00	3.33	1.33	1.33
	Max	2.33	3.33	4.33	0.67	7.33	14.67	10.67
		Total primary macroporosity	Total mouldic porosity	Total vuggy porosity	Other secondary macroporosity	Total secondary macroporosity	Total cement	Total replacive spar
BLA	Mean	1.70	9.90	1.13	0.13	11.17	12.00	9.93
	Min	0.00	1.33	0.00	0.00	2.99	1.33	0.00
	Max	10.33	26.67	3.33	0.67	26.67	28.00	19.00
OLA	Mean	2.05	6.00	1.71	0.14	7.86	6.09	8.48
	Min	0.00	2.00	0.00	0.00	3.34	0.33	1.00
	Max	6.67	12.67	4.33	0.33	13.00	14.67	22.33
RLA	Mean	1.57	9.72	2.57	0.48	12.77	9.03	17.67
	Min	0.00	1.67	0.00	0.00	2.33	0.67	0.00
	Max	13.00	20.33	12.33	2.33	28.33	22.00	43.33

Table 2, Average, minimum and maximum volumes of macropores, cement and replacive spar based on modal analysis of 42 samples. All values are percentages

Sample		G1	M1	M2	L1	G1	M-1
Scanner		Custom Bay				Micro-XCT	
Magnification		39.56	21.05	15.84	20.31	10	10
Image size (μm)		1000 x 641 x 183	572 x 431 x 611	931 x 851 x 594	711 x 551 x 701	706 x 398 x 578	412 x 663 x 817
Number of pores		1409	6583	83086	176091	101500	206481
Bulk volume (μm^3)		1.65E+10	1.47E+11	1.16E+12	3.09E+11	2.13E+09	2.44E+09
Pore volume (μm^3)		1.30E+07	1.34E+09	2.97E+10	2.14E+10	1.87E+08	6.46E+07
Imaged porosity (%)		0.08	0.91	2.56	6.92	8.79	2.65
Core porosity (%)		34.4	35.6	30.0	23.0	34.4	35.6
Kh (mD)		13.9	5.2	23.48	34.5	13.9	5.2
Unresolved porosity (% of total pores)		99.8	97.4	91.5	69.9	74.5	92.6
3D equivalent diameter (μm)	Min	6.45	12.4	1.67	12.9	2.9	2.8
	Mean	15.7	42.8	15.2	26.8	7.1	5.3
	Max	167	753	1230	104	222	154
Dominant pore size (μm)		39.9	39.8	49.6	29.5	5.32	4.37
Specific surface area (μm^{-1})	Min	0.064	0.023	0.012	0.029	0.129	0.114
	Mean	0.431	0.192	0.140	0.213	0.983	1.120
	Max	0.578	0.300	0.136	0.290	1.270	1.350
Aspect ratio	Min	1	1	1	1	1.00	1.00
	Mean	1.67	1.82	1.81	1.88	1.73	1.68
	Max	5.21	14.9	9.61	7.9	8.69	6.85
Tortuosity		34.6	10.9	4.77	3.22	3.46	5.52
Pore EqRadius (μm)	Min	3.23	6.2	8.37	6.44	1.46	1.38
	Mean	7.85	21.4	27.6	17.2	3.53	2.65
	Max	83.5	277	614	520	111.0	76.9
Co-ordination number	Min	1	1	1	1	1.00	1.00
	Mean	1.08	1.47	1.49	2.41	2.49	2.14
	Max	5	196	142	815	1105	406

Table 3 Pore geometrical data obtained by X-ray CT analysis

Sample		G1	M1	M2	L1
Scanner		ESEM			
Magnification		2000	5000	5000	5000
Image size (μm)					
Number of pores		124	228	288	228
Bulk area (μm^2)		2830	1576	1558	1337
Pore are (μm^2)		1149	533	286	530
Imaged porosity (%)		40.59	33.81	18.34	39.64
Core porosity (%)		34.4	35.6	30.0	23.0
Kh (mD)		13.9	5.2	23.48	34.5
Unresolved porosity (% of total porosity)		-18.0	5.02	38.87	-72.35
3D equivalent diameter (μm)	Min	0.0309	0.0252	0.0252	0.0178
	Mean	0.686	0.458	0.315	0.502
	Max	10.9	5.33	4.01	9.74
Dominant pore size (μm)		0.329	0.339	0.267	0.357
Perimeter over area (μm^{-1})	Min	0.869	1.92	1.89	1.45
	Mean	20.2	16.9	20.2	29.1
	Max	58.6	62	63	101
Aspect ratio	Min	1	1	1	1
	Mean	1.91	1.93	1.88	1.87
	Max	5.49	5	5.19	4.56
Tortuosity		1.22	2	2.8	5.74
Mini Feret Diameter (μm)	Min	0.052	0.044	0.045	0.036
	Mean	1.46	0.981	0.618	1.02
	Max	28.2	16.4	10	27.4

Table 4 Pore geometrical data obtained by ESEM

